Monthly Notices
of the
ROYAL ASTRONOMICAL SOCIETY

MNRAS **547**, 1–30 (2026) https://doi.org/10.1093/mnras/stag448
Advance Access publication 2026 March 6

MANGOS – II. Five new giant planets orbiting low-mass stars

G. Dransfield,[1,2,3★†] M. Timmermans,[3,4★†] D. Sebastian,[5] B. V. Rackham,[6,7] A. Burgasser,[8] K. Barkaoui,[9,4,6] A. H. M. J. Triaud,[3] M. Gillon,[4] J. M. Almenara,[10,11] S. L. Casewell,[12] K. A. Collins,[13] A. Fukui,[14,15] C. Janó Muñoz,[16] S. Kanodia,[17] N. Narita,[9,14,15] E. Palle,[9,18] M. G. Scott,[3] A. Soubkiou,[4] A. Stokholm,[3] J. Audenaert,[7] G. Á. Bakos,[19] Y. Beletsky,[17] Z. L. de Beurs,[6,20] Z. Benkhaldoun,[21,22] A. Burdanov,[6] R. P. Butler,[17] D. Caldwell,[23] J. D. Crane,[24] Y. T. Davis,[3] B. O. Demory,[25] E. Ducrot,[26,27] Y. Gómez Maqueo Chew,[28] M. Gachaoui,[4,22] J. D. Hartman,[19] M. J. Hooton,[16] E. Jehin,[29] S. Mercier,[6] F. Murgas,[9,18] C. Murray,[30] P. P. Pedersen,[16,31] F. J. Pozuelos,[32] M. Rice,[33] G. Ross,[19] S. A. Shectman,[24] E. Softich,[8] M. Tala Pinto,[34] A. M. Vanderburg,[7] J. Villasenor,[7] J. de Wit[6] and S. Zúñiga-Fernández[4]

Affiliations are listed at the end of the paper

Accepted 2026 March 3. Received 2026 March 2; in original form 2025 October 13

ABSTRACT

Giant planets orbiting low-mass stars on short orbits present a conundrum, as in the most extreme cases their existence cannot be reconciled with current models of core accretion. Therefore, surveys dedicated to finding these rare planets have a key role to play by growing the sample to overcome small number statistics. In this work, we present MANGOS, a programme dedicated to the search for giant objects (planets, brown dwarfs, and low-mass stars) orbiting M dwarfs. We report on the discovery of five new giant planets (TOI-3288 Ab, TOI-4666 b, TOI-5007 b, TOI-5292 Ab, TOI-5916 b) first detected by *TESS*, and confirmed using ground-based photometry and spectroscopy. The five planets have radii in the range of 0.99–1.12 R_{Jup}, masses between 0.49 and 1.69 M_{Jup}, and orbital periods between 1.43 and 2.91 d. We reveal that TOI-3288 and TOI-5292 are wide binaries, and in the case of TOI-5292, we are able to characterize both stellar components. We demonstrate that the planets presented are suitable for further characterization of their obliquities and atmospheres. We detect a small but significant eccentricity for TOI-5007 b, although for this to be more robust, more observations are needed to fully sample the orbit. Finally, we reveal a correlation between stellar metallicity and planet bulk density for giant planets orbiting low-mass stars.

Key words: exoplanets – planets and satellites: detection – planets and satellites: formation – planets and satellites: fundamental parameters.

1 INTRODUCTION

Prior to the detection of the first exoplanet orbiting a Sun-like star (M. Mayor & D. Queloz 1995), the nature and locations of all eight known planets orbiting a main-sequence star were adequately reproduced by the accepted planetary formation models of the day (J. J. Lissauer 1993). 51 Peg b was thus the first planet to spoil the fun.

In the decades since, over 6000 exoplanets have been detected,[1] most of which also belong to emerging populations not seen in the Solar system. The hot Jupiter population in particular consists of giant planets (defined here as having $R_p \geq 7R_\oplus$) with orbital periods $P < 10$ d, resulting in equilibrium temperatures hotter than 1000 K. Thanks to their large sizes and short orbital periods, hot Jupiters produce easily detectable signals in photometry, radial velocity (RV) and both transmission and emission spectroscopy, making them one of the best-studied populations.

Despite this, the puzzle of their formation remains unsolved. Current formation theory of giant planets indicates that the standard core accretion model (e.g. J. B. Pollack et al. 1996; Y. Alibert et al. 2005; B. Liu & J. Ji 2020) is the most likely formation path-

---

★ E-mail: george.dransfield@physics.ox.ac.uk (GD); m.timmermans@bham.ac.uk (MT)

† These two authors contributed equally to this work and should be considered joint first authors.

[1] According to the NASA Exoplanet Archive, accessed on UTC 2025 Sep 25.

way. However, there is still no consensus on whether formation takes place '*in situ*' (e.g. K. Batygin, P. H. Bodenheimer & G. P. Laughlin 2016; A. C. Boley, A. P. Granados Contreras & B. Gladman 2016) or beyond the ice line where there are more solids available (R. R. Rafikov 2006; A.-M. A. Piso, A. N. Youdin & R. A. Murray-Clay 2015). In the latter case, planets would then need to migrate toward their present-day positions (e.g. S. Ida & D. N. C. Lin 2004; Y. Alibert et al. 2005), which could happen via disc migration (D. N. C. Lin, P. Bodenheimer & D. C. Richardson 1996; C. Baruteau et al. 2014) or high-eccentricity tidal migration (F. A. Rasio & E. B. Ford 1996).

Large numbers of hot Jupiters were discovered in the early days of the field; however, RV surveys estimated the occurrence rate for this population to be of the order of 1 per cent for FGK stars (e.g. J. T. Wright et al. 2012). This occurrence rate is consistent with the results from population synthesis models (A. Emsenhuber et al. 2021).

But what of M dwarfs? They constitute the most abundant stellar population in the galaxy (accounting for 60–70 per cent of all stars; T. J. Henry et al. 2006; C. Reylé et al. 2021), and host on average 1–2 planets each (I. Ribas et al. 2023). Given that on average the mass of a protoplanetary disc scales with stellar mass (S. M. Andrews et al. 2013), and low-mass stars have longer Keplerian time-scales (G. Laughlin, P. Bodenheimer & F. C. Adams 2004), giant planet occurrence rate is expected to decrease with stellar mass. This prediction is supported by the population synthesis models of R. Burn et al. (2021), which also found that no giant planets were formed around stars with $M_\star < 0.5\mathrm{M}_\odot$. However, recent observation-driven occurrence rates have been calculated based on the *TESS* mission data. T. Gan et al. (2023) find an occurrence rate for giant planets with $P < 10$ d of 0.27 ± 0.09 per cent for stellar masses between 0.45 and 0.65 $\mathrm{M}_\odot$. This is in agreement with E. M. Bryant, D. Bayliss & V. Van Eylen (2023), who found that giant planets occur at a rate of 0.29 ± 0.15 per cent, 0.108 ± 0.083 per cent, and 0.137 ± 0.097 per cent, for stellar hosts with $M_\star = 0.42$–$0.71\ \mathrm{M}_\odot$, 0.26–$0.42\ \mathrm{M}_\odot$, and 0.088–$0.26\ \mathrm{M}_\odot$, respectively. R. I. Glusman et al. (2025) extended this work to include more recent data, finding slightly lower occurrence rates of 0.067 ± 0.047 per cent 0.139 ± 0.069 per cent, and 0.032 ± 0.032 per cent for a median stellar mass of 0.54, 0.35, and $0.18\mathrm{M}_\odot$, respectively. Given the model predictions of R. Burn et al. (2021) that no giant planets should form around hosts with $M_\star < 0.5\mathrm{M}_\odot$, these small but non-zero measured occurrence rates around the lowest-mass stars present a conundrum.

Thus far, 32 short period giant planets with $P < 10$ d have been discovered orbiting M dwarfs, with hosts ranging from 0.2 to 0.7 $\mathrm{M}_\odot$ (e.g. C. I. Cañas et al. 2022; S. Kanodia et al. 2025). Among those, six orbit stars around mid to late M dwarfs with $M_\star < 0.4\mathrm{M}_\odot$: TOI-3235 b (M. J. Hobson et al. 2023), TOI-5205 b (S. Kanodia et al. 2023), TOI-7149 b (S. Kanodia et al. 2025), TOI-4860 b (A. H. M. J. Triaud et al. 2023), TOI-519 b (H. Parviainen et al. 2021a; T. Kagetani et al. 2023), and TOI-6894 b (E. M. Bryant et al. 2025). These discoveries showcase the need to re-evaluate formation theories for these objects. One alternative pathway to core accretion to have been proposed for low-mass stars is gravitational instability (A. P. Boss 1997, 2006; A. P. Boss & S. Kanodia 2023). However, A. Mercer & D. Stamatellos (2020) have shown that this mechanism, where planets form from the collapse of a gravitationally unstable disc, should produce planets of masses larger than $2\mathrm{M}_{\mathrm{Jup}}$. Only six super-Jupiter mass planets in our parameter space of interest have been found, which are excellent test cases to reconcile theory and observations: TOI-4201 b (M. Delamer et al. 2024), TOI-2379 b, TOI-2384 b (E. M. Bryant et al. 2024), TIC 46 432 937 b (J. D. Hartman et al. 2024), TOI-6303 b, and TOI-6330 b (A. Hotnisky et al. 2025). The latter is the most massive planet to have been found orbiting an M star with a mass of $10.0 \pm 0.3\mathrm{M}_{\mathrm{Jup}}$.

While the mass of TOI-6330 b is remarkably large, it is still below the deuterium burning limit that defines brown dwarfs (BDs), canonically found in the mass range $13\mathrm{M}_{\mathrm{Jup}} \lesssim M_{\mathrm{BD}} \lesssim 80\mathrm{M}_{\mathrm{Jup}}$ (G. Chabrier et al. 2014). The occurrence rate of BDs as companions to FGK stars on short orbits is low (e.g. D. Grether & C. H. Lineweaver 2006), with values as low as 0.56 per cent estimated from RV surveys (N. Grieves et al. 2017), and this paucity inside 10 AU is known as the 'brown dwarf desert' (e.g. J. Sahlmann et al. 2011). Brown dwarf companions orbiting around low-mass stars are even rarer than giant planets, with only 12 transiting BDs confirmed thus far (e.g. J. Maldonado et al. 2023; K. Barkaoui et al. 2025b; T. Gan et al. 2025b). Studying BDs around low-mass stars is also crucial to understand the formation environment around these stars. It is also unclear whether the 'dryness' and 'width' of the so-called brown dwarf desert are determined by companion mass or mass ratio. Thus, discovering and characterizing BD companions to M dwarfs on short orbits adds critical pieces to the puzzle of giant planet formation and low-mass stars as planet hosts.

In all cases, the characterization of planets and BDs is fundamentally constrained by the accuracy of the stellar parameters of their host stars. Stellar properties such as mass and radius provide the basis for deriving the orbital and physical parameters of the associated planets. For single stars, we use evolutionary stellar models such as I. Baraffe et al. (2015) to derive stellar parameters. However, several works have shown that observed radii of M dwarfs were inflated compared to those expected from benchmark models (e.g. L. Casagrande, C. Flynn & M. Bessell 2008; F. Spada et al. 2013). Multiple hypotheses are considered to explain this phenomenon, such as stellar magnetic activity inhibiting convection and producing stellar spots which can cause an under- or overestimation of the eclipse depth of the binary (J. C. Morales et al. 2010; G. A. Feiden & B. Chaboyer 2013), or stellar metallicity which affects the opacity of the outer layers of the star (D. H. Berger et al. 2006; A. Boetticher et al. 2019). This radius inflation can significantly impact inferences of key planetary parameters. In order to increase the statistical significance of empirical scaling relations such as the ones of A. W. Mann et al. (2015) and A. W. Mann et al. (2019), it is critical to add to the sample of low-mass stars with absolute mass and radius measurements, i.e. low-mass double-lined eclipsing binaries. These objects can mimic the photometric behavior of giant planet candidates when looking at M dwarfs since the companion star would be of equal or lower mass. Notably, the eclipsing binaries with low mass (EBLM) project (A. H. M. J. Triaud et al. 2013) has provided absolute physical parameters of dozens of low-mass binaries (e.g. D. Sebastian et al. 2023; M. I. Swayne et al. 2024), and applied high-resolution cross-correlation techniques to deal with extreme flux ratios, effectively turning single-lined eclipsing binaries into double-lined ones (D. Sebastian et al. 2025).

In this context, we present MANGOS (**M** dwarfs **A**ccompanied by close-i**N** **G**iant **O**rbiters with **S**PECULOOS), a comprehensive program designed to detect, catalogue, and characterize giant companions orbiting low-mass stars. The MANGOS initiative encompasses three main scientific cases: giant planets, brown dwarfs, and double-lined eclipsing binaries. This project was first presented in A. H. M. J. Triaud et al. (2023), where we reported the discovery of TOI-4860 b, a Jupiter-sized planet orbiting an M4.5 host. In the present work, we report on the discovery, confirmation and characterization of five new MANGOS planets, orbiting hosts with masses 0.48–0.67$M_\odot$.

Our paper is structured as follows. We begin in Section 2 by describing the MANGOS programme strategy for planets. We then describe our full photometric and spectroscopic observing campaigns in Section 3. In Section 4, we characterize our host stars, followed by a global analysis of all available data in Section 5. We present a summary of key resulting parameters in Section 6, which we discuss in the context of the field in Section 7. Finally, we conclude in Section 8.

2 THE MANGOS STRATEGY

As described above, MANGOS is a holistic programme of discovery and characterization of giant objects hosted by low-mass stars. The three strands of the programme (giant planets, brown dwarf-M dwarf binaries, and M dwarf-M dwarf binaries) fall under two sub-programmes: planetary follow-up and binary characterization. All new MANGOS targets are initially treated as planetary candidates; however, those found to be binaries are switched to the binary programme. In this section, we describe the steps taken to validate and confirm MANGOS planets, as well as what sets this project apart from others.

2.1 MANGOS planet candidate selection and validation workflow

All targets in the MANGOS sample come from the list of *TESS* Objects of Interest (TOIs; N. M. Guerrero et al. 2021). We begin our cuts by selecting candidates orbiting hosts with $T_{\text{eff}} \leq 4000$ K, to ensure all low-mass stars are captured up to M0. We then rule out any TOIs with radii $R_\text{p} < 7\,\text{R}_\oplus$ and periods $P > 7$ d to select only close-in giant planet candidates.

Due to the faintness of many of the hosts, the photometric precision on the *TESS* light curves is often limited, leading to low signal-to-noise ratio (SNR) detections of candidate events. Additionally, the large pixel scale of *TESS* of 21 arcsec often leads to multiple sources in the apertures used to extract the photometry. In the case of crowded stellar fields, the probability of false positives increases. To ensure the transit event is indeed on the target star, a first vetting step is to observe a transit with the TRAPPIST (TRAnsiting Planets and PlanetesImals Small Telescope) telescopes. TRAPPIST-South (TS, M. Gillon et al. 2011; E. Jehin et al. 2011) is located at ESO La Silla Observatory in Chile. It is a 0.6-m telescope equipped with a FLI ProLine PL3041-BB camera and a back-illuminated CCD. The pixel size is 0.64 arcsec, providing a total field of view of 22 arcmin × 22 arcmin, for an array of 2048 × 2048 pixels. TRAPPIST-North (TN; K. Barkaoui et al. 2019) is a twin of its Southern counterpart located at Oukaïmeden Observatory in Morocco. It is equipped with a thermoelectrically cooled 2K×2K Andor iKon-L BEX2-DD CCD camera with a pixel scale of 06 arcsec and a field of view of 20 arcmin × 20 arcmin. Both TS and TN are Ritchey-Chrétien telescopes with F/8 equipped with German equatorial mounts. For the purpose of the MANGOS programme, our observations with TRAPPIST are conducted in the $I + z$ filter, a custom filter optimized for low-mass stars with a transmittance >90 per cent from 750 nm to beyond 1000 nm.

At the end of this first step, the transit is confirmed on target and its ephemeris is corrected if needed. The candidates are then added to our programmes for reconnaissance spectroscopy for host characterization using optical and infrared spectrographs (see Section 3.2). This step allows us to refine stellar parameters, as well as check for spectroscopic indicators of youth or binarity.

Further transit observations are then scheduled on the SPECULOOS (Search for habitable Planets EClipsing ULtra-cOOl Stars) telescopes to carry out multi-colour photometric validation. The SPECULOOS-South Observatory (SSO, L. Delrez et al. 2018; D. Sebastian et al. 2021) is located at ESO Paranal Observatory in Chile. It is composed of four identical 1.0m F/8 Ritchey-Chrétien telescopes, named after the Galilean moons Io, Europa, Ganymede, and Callisto. All telescopes are equipped with a deep-depletion Andor iKon-L $2k \times 2k$ CCD camera, resulting in a total field of view of 12 arcmin for a pixel scale of 0.35 arcsec (A. Burdanov et al. 2018). Recently, SSO/Callisto was equipped with the SPECULOOS Infra-Red photometric Imager for Transits (SPIRIT). It is an InGaAs CMOS-based instrument with a custom wide-pass filter, zYJ, covering the wavelength range 0.81–1.33 μm to minimize the effect of precipitable water vapor on differential light curves (P. P. Pedersen et al. 2024; C. Janó Muñoz et al. 2025). SPIRIT has a 1024 × 1280 detector with 12-μm pixels, yielding a 5.3 arcmin × 6.6 arcmin field of view.

Two facilities cover the northern hemisphere: the SPECULOOS-North Observatory (SNO; A. Y. Burdanov et al. 2022), which hosts one telescope named Artemis, and SAINT-EX (Search And characterization of Transiting EXoplanets; B. O. Demory et al. 2020). Both are twins of the SSO telescopes equipped with identical cameras. SNO is located at Teide Observatory in Tenerife while SAINT-EX is located at the National Astronomical Observatory of Mexico, in San Pedro Mártir. In total, six telescopes may be used to check for a chromatic signature of the transit depths of the MANGOS candidates, a telltale sign of binarity. False positive scenarios could be either an unresolved background blend with our target or another smaller, redder star (or BD) orbiting the target. The chromaticity investigation towards the bluer bands identifies any additional dilution of the transit signal due to a non-opaque orbiting body in the considered wavelength ranges. We also schedule observations at phase 0.5 in our reddest filter available to check for hints of a secondary eclipse.

We then carry out statistical validation using the `TRICERATOPS` (S. Giacalone et al. 2021) package, a Bayesian framework to evaluate the flux of nearby stars and assess the false positive probabilities (FPPs). While this is a standard step in our workflow, MANGOS planet candidates will often have high FPPs as many of them present a grazing configuration. In the case of small planets orbiting larger stars, a grazing transit is very often an indicator of binarity, but due to the much larger radius ratios in our sample, we expect to find a higher proportion of truly grazing planets.

The most promising targets will then be proposed for RV measurements on suitable facilities. Given the faintness of the targets and the high expected RV signals, ESPRESSO and MAROON-X allow us to achieve excellent precision on mass measurements with only a handful of spectra. In this paper, we present planets found in our successful ESPRESSO programmes during P112 and P114 (P112.25ZF, PI: G. Dransfield; P114.27JF, PI: M. Timmermans). Through our membership of the TFOP (*TESS* Follow-up

Observing Programme) collaboration, our data are supplemented by observations taken by LCO, MuSCAT2, ExTrA, and PFS.

2.2 The MANGOS advantage

The TRAPPIST and SPECULOOS facilities are the primary photometric instruments used for the MANGOS programme. Together, they total three instruments in the northern hemisphere (TN, SNO, and SAINT-EX), and five in the southern one (the four SSO telescopes, and TS). All are optimized in the near-infrared for low-mass stars but extend into the optical down to 350 nm. Having multiple identical telescopes observing simultaneously a transit event generates a more robust detection of chromatic depth variations than at different epochs using different facilities. Notably, the SPIRIT camera allows us to explore up to 1.3 µm, a regime where secondary eclipses could be detected for hot orbiting bodies. When that is the case, we can determine the brightness temperature of the hottest MANGOS candidates or reveal a binary. Finally, our simultaneous multicolour photometry approach also makes it possible to capture the chromaticity of any flares and stellar spots, in turn permitting a direct characterization of these activity indicators. This is particularly valuable in the case of M dwarf stars as they tend to be very active.

3 OBSERVATIONS

In this section, we describe the observations collected to characterize the five host stars, as well as to confirm the planetary nature of the giant planets orbiting them. We begin by describing the photometric data collected from space and the ground, followed by the spectroscopic datasets from six different optical and near-infrared instruments. A journal of photometric observations can be found in Tables B1 and B2.

3.1 Photometry

In this section, we describe the photometric data collected for the five targets presented in this work. In Section 3.1.1, we describe the initial target identification by *TESS*, as well as the available data. The remaining sections describe ground-based photometric data collection.

We note that our scrutiny of archival imaging and *Gaia*, described in Section 4.1, revealed both TOI-3288 and TOI-5292 to have bound companions. We therefore refer to them as TOI-3288 AB and TOI-5292 AB where observations are unable to separate the components, and TOI-3288 A or B and TOI-5292 A or B where observations resolve the individual stars.

3.1.1 TESS

All five targets considered in this work were initially found by the *TESS* mission. For all, threshold crossing events (TCEs) were detected and Data Validation (DV) reports were created from the Science Processing Operations Center (SPOC; J. M. Jenkins et al. 2016) pipeline or Quick Look Pipeline (QLP; C. X. Huang et al. 2020) depending on the cadence of the data taken. The DV reports a series of validation and diagnostic tests to evaluate the confidence in the transit events from the TCE alert, they are described in J. D. Twicken et al. (2018) and J. Li et al. (2019) for SPOC detections and N. M. Guerrero et al. (2021) for QLP detections[2] For all candidates, the DV reports associated with the initial detections show the signals pass all the vetting steps apart from TOI-5007.01, which showed some odd/even transit depth variations in the initial QLP detection DV report. This variation can be attributed to the crowded field with many neighbouring stars contaminating the *TESS* aperture, resulting in poor data quality for the Sector 39 initial detection. A subsequent SPOC detection in Sector 65 did not show such odd/even variations. The typical apertures used to extract the photometry in the *TESS* pixel files are given in Fig. A1, and the *TESS* data is described below.

TOI-5007 (TIC 424196109) was observed in Sectors 12, 39, and 65 with full-frame image (FFI) data (1800, 600, and 200 s, respectively) and also with 2-min cadence data in Sector 65. TOI-5007.01 was initially detected in Sector 39 by the QLP faint-star search (M. Kunimoto et al. 2022) on UTC 2022 Jan 6. The planet candidate had a radius of $10.62 \pm 0.96\,R_{\oplus}$, for a transit depth of 21300 ± 157 ppm and a period of 2.5433 ± 0.0007 d. We obtained the Simple Aperture Photometry and Presearch Data Conditioning Simple Aperture Photometry (SAP; PDCSAP; J. C. Smith et al. 2012; M. C. Stumpe et al. 2012, 2014) flux available for the 2-minute cadence data of Sectors 65 from the NASA Mikulski Archive for Space Telescopes (MAST) using the `Lightkurve` package (Lightkurve Collaboration et al. 2018). The PDCSAP flux is produced by the SPOC pipeline where it is corrected for instrumental systematics as well as dilution of the signal due to crowding of the aperture. However, upon analysing the data combined with uncontaminated ground-based light curves, we find a better fit to the data with the SAP flux paired to a free dilution factor. The short-cadence data offers a much better precision than the QLP data which is why we selected this data product for our transit analysis.

TOI-5292 AB (TIC 33397739) was observed in Sectors 42, 70, and 92 with FFI data (600s and 200s), and 2-min cadence data were also taken in Sectors 70 and 92. TOI-5292.01 was detected in Sector 42 by the QLP faint-star search on UTC 2022 Aug 22. A depth of 44030 ± 913 ppm was reported for a 2.0231 ± 0.0007 day period, corresponding to a planet with a radius of $13.43 \pm 2.00\,R_{\oplus}$. For the global analysis, similarly to TOI-5007, we used the PDCSAP flux of Sectors 70 and 92 obtained from the SPOC pipeline.

TOI-5916 (TIC 305506996) was observed in Sector 55 with an exposure of 600s and in Sector 82 with exposures of 200s and 120s. The candidate TOI-5916.01 was also first detected by the QLP faint-star search in Sector 55 on UTC 2022 Nov 8. The DVR reports a planet candidate of a size of $10.92 \pm 0.60\,R_{\oplus}$ and a period of 2.3682 ± 0.0007 d, for a transit depth of 48700 ± 3699 ppm.

TOI-3288 AB (TIC 79920467) was observed in Sectors 13 and 27 of *TESS* with FFI data (1800 and 600 s, respectively), and 67 with both 2-min cadence and FFI data (120 and 200s). The planet candidate TOI-3288.01 detection was made on UTC 2021 Jun 4 by the QLP pipeline faint-star search in Sector 13 and 27. It reported a 31360 ± 8 ppm deep transit at a period of 1.4339 ± 0.0001 d, corresponding to a $12.38 \pm 0.42\,R_{\oplus}$ planet. Finally, TOI-4666 (TIC 165202476) was only observed in Sector 31 with FFI data data (600 s). The detection of the 2.9094 ± 0.0002 d period and 45160 ± 16 ppm deep signal was made on UTC 2021 Dec 21, corresponding to a planet radius of $12.87 \pm 0.47 R_{\oplus}$. This signal was also found through QLP's faint-star search. Both of these last two systems are also confirmed by another team (Y. G. C. Frensch et al. 2025). Through coordination with them, we agreed

---

[2] The DV reports are available at https://tev.mit.edu/.

not to use the *TESS* data in our analyses in order to report fully independent results. The 120 s cadence *TESS* data used in the analyses for TOI-5007, TOI-5292 A, and TOI-5916 are shown in Fig. 1.

3.1.2 *TRAPPIST*

We scheduled the *TESS* follow-up observations using the *TESS* Transit Finder based on the `Tapir` interface (E. Jensen 2013). The data is then processed using a custom pipeline built with the `prose` package, a publicly available `python` framework for processing astronomical images[3] (L. J. Garcia et al. 2021; L. Garcia et al. 2022). This pipeline provides standard data reduction as well as photometric extraction.

We observed a full transit TOI-5916.01 with TN on UTC 2022 Nov 28 in the $I+z$ band and with an exposure time of 120 s. Full width at half-maximum (FWHM) for this observation was 2.27 arcsec. This was observed simultaneously with the SNO/Artemis (described above).

A full transit of TOI-3288.01 was observed with TS on UTC 2023 Sep 12 in the $I+z$ band with an exposure time of 60 s and an FWHM of 2.87 arcsec.

We observed a full transit of TOI-4666.01 with TS on UTC 2023 Jan 17 (simultaneous observation with SSO, described above) in *Sloan-z'* with an exposure of 130 s and an FWHM of 2.52 arcsec. A second full transit event was observed with TS on UTC 2024 Dec 18 in *Sloan-z'* with an exposure of 120 s and an FWHM of 2.32 arcsec.

TOI-5292.01 was observed for the first time with TN on UTC 2023 Dec 09 in $I+z$, where only the transit egress was detected. The observation was taken with 120 s exposures and had an FWHM of 2.13 arcsec. On UTC 2023 Dec 11, a full transit was observed with TN in *Sloan-z'* with exposures of 150 s and an FWHM of 2.43 arcsec.

We observed a full transit of TOI-5007.01 with TS on UTC 2022 May 02 in $I+z$ with an exposure of 60 s and FWHM of 1.93 arcsec. Second and third full transits were observed on UTC 2022 Jul 02 and UTC 2022 Feb 03 with exposure = 110 s and in bands $I+z$ and *Sloan-z'*, respectively.

3.1.3 *SPECULOOS*

All SPECULOOS observations are scheduled using SPECULOOS's custom scheduler SPOCK[4] (D. Sebastian et al. 2021), and initially processed by an automatic data reduction pipeline, described in C. A. Murray et al. (2020). Successful observations of *TESS* targets are then reprocessed manually using a custom pipeline built with the `prose` package. This allows for a better control over the various parameters of the differential photometry process, namely free control over the background annulus size as well as photometric apertures and choice of comparison stars. This is critical in the case of TOI-5007 b where the field is very crowded.

We collected 17 observations of TOI-3288.01 with SSO on nine different nights, between UTC 2022 Jun 30 and UTC 2025 Sep 15. Exposure times ranged from 18 s for observations in *zYJ*, to 120 s for those collected in *Sloan-g'*. We collected one observation at phase 0.5 on UTC 2022 Aug 07 wtih SSO in $I+z$ and did not observe a secondary eclipse.

We collected 11 observations of TOI-4666.01 across 6 nights with SSO between UTC 2022 Oct 10 and UTC 2024 Dec 18, using exposure times of 16–160 s. We observed at phase 0.5 on UTC 2023 Sep 08 and UTC 2023 Oct 13 in $I+z$ and *Sloan-i'* and did not detect a secondary eclipse.

We collected four transit observations TOI-5007.01 across three nights with SSO, between UTC 2022 Aug 27 and UTC 2025 Mar 12 using 23–120 s exposures.

We obtained three transit observations of TOI-5292.01 with SNO over three nights, between UTC 2024 Sep 27 and UTC 2024 Dec 19 using exposure times between 60 s (for *Sloan-z'*) and 160 s (*Sloan-g'*). We collected one further observation at phase 0.5 on UTC 2024 Dec 18 and ruled out a secondary eclipse event.

We observed TOI-5916.01 on the night of UTC 2022 Nov 28 with SNO using the *Sloan-g'* filter with a 14 s exposure.

3.1.4 *MuSCAT2*

TOI-5916 was observed on the night of UTC 2024 Aug 16 using the multiband imager MuSCAT2 (N. Narita et al. 2019), mounted on the 1.5 m Telescopio Carlos Sánchez (TCS) at Teide Observatory, Spain. MuSCAT2 is equipped with four CCDs, allowing for simultaneous imaging in the g', r', i', and z_s bands with minimal readout time. Each CCD consists of 1024 × 1024 pixels, covering a field of view of 7.42.13 arcmin × 7.42.13 arcmin.

The observations were conducted with the telescope in nominal focus. The exposure times were set to 50 s for the g', r', and z_s bands, and 15 s for the i' band. The raw data were processed using the MuSCAT2 pipeline (H. Parviainen et al. 2019), which performs dark and flat-field calibrations, aperture photometry, and transit model fitting while accounting for instrumental systematics.

3.1.5 *ExTrA*

The Exoplanets in Transits and their Atmospheres (ExTrA, X. Bonfils et al. 2015) is a low-resolution near-infrared (0.85–1.55 μm) multiobject spectrograph fed by three 60-cm telescopes located at La Silla Observatory in Chile. Eleven transits of TOI-5007.01 were observed using one, two, or three of the ExTrA telescopes. We used 8 arcsec aperture fibres and the lowest resolution mode ($R\sim 20$) of the spectrograph, a combination that is optimal for the target's magnitude, with an exposure time of 60 s. Five fibers are positioned in the focal plane of each telescope to select light from the target and four comparison stars. The resulting ExTrA data were analysed using custom data reduction software described in M. Cointepas et al. (2021).

3.1.6 *LCO-SSO-0m4*

We observed an ingress of TOI-5007.01 from the (LCOGT; T. M. Brown et al. 2013) 0.4 m network node at Siding Spring Observatory near Coonabarabran, Australia (SSO). The telescope is equipped with a 2048 × 3072 pixel SBIG STX6303 camera having an image scale of 0.57 arcsec pixel^{-1}, and a FOV of 19 arcmin × 29 arcmin. The observation was carried out on UTC 2023 Apr 21 in the Sloan-r' with an exposure time of 600s. Science images were calibrated by the standard LCOGT BANZAI pipeline (C.

---

[3] https://github.com/lgrcia/prose

[4] https://github.com/educrot22/SPOCK_v2/tree/main/SPOCK

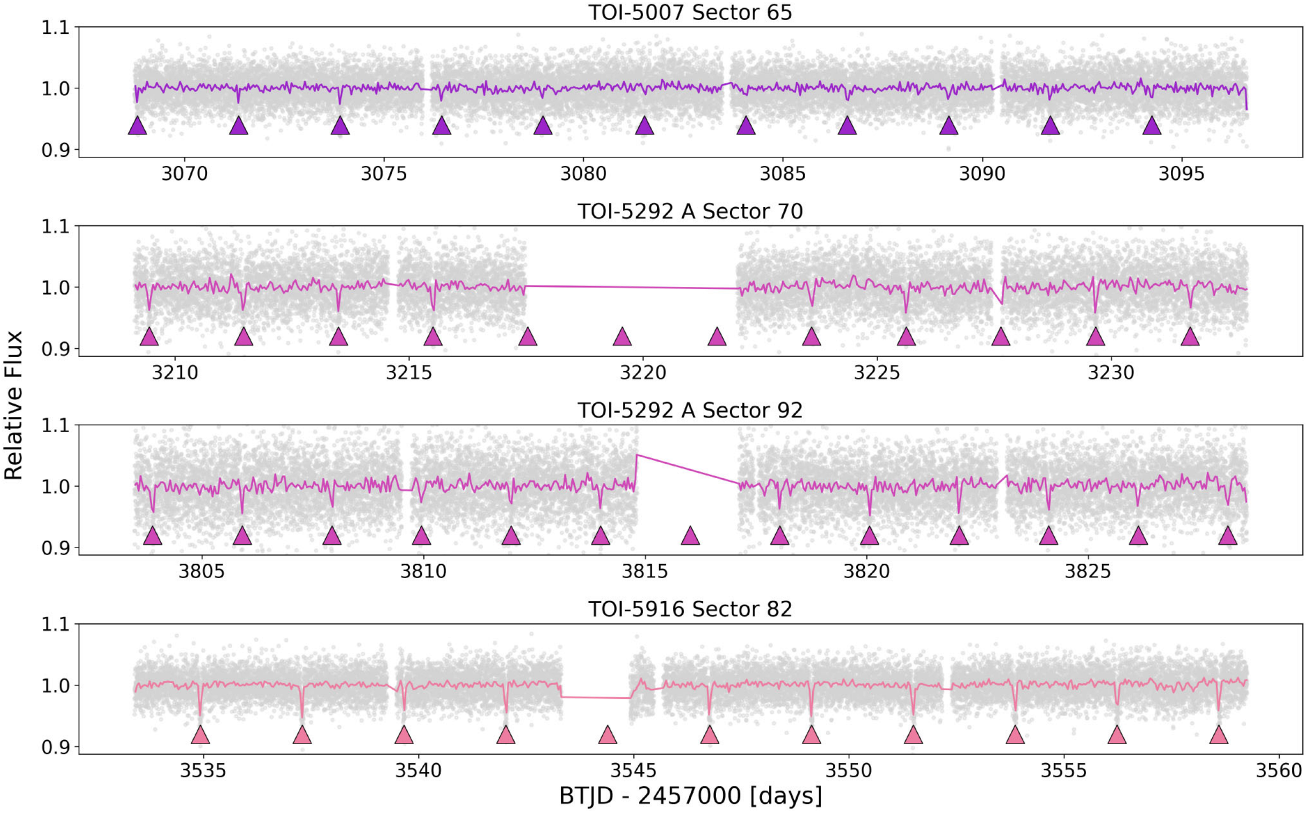

Figure 1. *TESS* 120 s cadence data of TOI-5007 (top), TOI-5292 A (middle), and TOI-5916 (bottom). In this cadence, TOI-5007 was observed in Sector 65, TOI-5292 A in Sectors 70 and 92, and TOI-5916 in Sector 82. Light grey points show the 120 s exposures, and the coloured lines show the flux in 1-h bins. The transit events of each planet candidate are indicated by coloured arrows.

McCully et al. 2018), and differential photometry was performed using AstroImageJ (AIJ) (K. A. Collins et al. 2017). The light curve was not included in the global fit due to the low SNR of the transit.

3.2 Spectroscopy

3.2.1 IRTF/SpeX

We obtained near-infrared spectra of two targets and one companion star with the SpeX spectrograph (J. T. Rayner et al. 2003) on the 3.2-m NASA Infrared Telescope Facility. The short-wavelength cross-dispersed (SXD) mode was used with the 0.3 arcsec × 15 arcsec slit aligned to the parallactic angle, yielding $R{\sim}2000$ spectra covering 0.80–2.42 µm. TOI-5292 A was observed on UTC 2023 Oct 31 under clear conditions with 0.6 arcsec seeing. We collected 12 exposures of 300 s at an average airmass of 1.1, nodding in an ABBA pattern. We observed its faint, bound companion located 9.42 arcsec away, 2MASS J22565386-0807049 (TOI-5292 B), on UTC 2025 Sep 12, collecting 12 × 300 s exposures under 1.6 arcsec seeing at an average airmass of 1.3. Finally, TOI-5916 was observed on UTC 2024 Jul 11 under 1.5 arcsec seeing. We again collected 12 × 300 s exposures at an average airmass of 1.0. After each science target, we collected a standard SXD calibration set and observed an A0 V standard at a similar airmass. The data were reduced with the Spextool v4.1 pipeline (M. C. Cushing, W. D. Vacca & J. T. Rayner 2004), following the standard approach (e.g. K. Barkaoui et al. 2024; M. Ghachoui et al. 2024; K. Barkaoui et al. 2025a). The final spectra of TOI-5292 A, TOI-5292 B, and TOI-5916 have median SNRs per resolution element of 78, 9, and 76, respectively.

3.2.2 SOAR/TripleSpec4.1

We collected medium-resolution near-infrared spectra of TOI-3288 A, TOI-4666, and TOI-5007 with the TripleSpec4.1 spectrograph (E. Schlawin et al. 2014) on the 4.1-m Southern Astrophysical Research (SOAR) telescope using the AEON queue. The fixed 1.1 arcsec slit provides $R{\sim}3500$ spectra covering 0.80–2.47 µm, and all observations were carried out with the slit aligned to the parallactic angle and nodding in an ABBA pattern. No significant contamination ($\lesssim$ 5 per cent of the total flux) is expected from TOI-3288 B, the bound companion at 2.16 arcsec, given this instrumental set up and the delta magnitude of 3.0 in the *Gaia* band. TOI-4666 was observed on UTC 2023 Oct 6 under 1.9 arcsec seeing at an airmass of 1.2, with eight 30-s exposures yielding a median SNR per resolution element of 56. TOI-3288 A and TOI-5007 were observed on UTC 2025 Jul 14 under 1.3 arcsec seeing at airmasses of 1.1 and 1.4, respectively, with four 120-s exposures for TOI-3288 A (median SNR per resolution element of 87) and four 300-s exposures for TOI-5007 (median SNR of 104).

For each target, we also observed an A0 V star at a similar airmass for telluric correction. The data were reduced with Spextool v4.1 (M. C. Cushing et al. 2004), modified for TripleSpec4.1[5], us-

---

[5] https://noirlab.edu/science/observing-noirlab/observing-ctio/observing-soar/data-reduction/triplespec-data

ing the standard set of flat-field and arc-lamp exposures collected closest to the observations.

3.2.3 *Lick/Kast*

We obtained low-resolution red optical spectra of TOI-5916 and TOI-5292 A and B with the Kast double spectrograph (J. S. Miller & R. P. S. Stone 1994) on the 3-m Shane telescope at Lick Observatory on UTC 2024 Dec 5 and UTC 2025 Aug 26, respectively. Observations in UTC 2024 Dec were obtained in partly cloudy conditions with 0.7 arcsec seeing; observations in UTC 2025 Aug were obtained in scattered clouds with 0.9 arcsec seeing. Both observations were conducted in a single longslit mask, with blue and red optical spectra split at 5700 Å by the d57 dichroic and dispersed by the 600/4310 grism and 600/7500 grating, respectively. TOI-5916 was observed using the 1 arcsec wide slit aligned to the parallactic angle to resulting in spectral resolutions of $\lambda/\Delta\lambda \approx 2200$ and ≈ 2900 for the blue and red spectra, respectively. We obtained a single 2400 s exposure in the blue channel and two 1200 s exposures in the red channel at an average airmass of 1.4. The G2 V star HD 211 476 ($V = 7.0$) was observed at an airmass of 1.2 for telluric absorption calibration, and the sdO spectrophotometric calibrator Feige 110 (M. Hamuy et al. 1992, 1994) was observed afterward for flux calibration. TOI-5292 A and B were observed using the 1.5 arcsec wide slit aligned to the binary axis (position angle 232^o), resulting in spectral resolutions of $\lambda/\Delta\lambda \approx 1500$ and ≈ 1950 for the blue and red spectra, respectively. We obtained a single 3600 s exposure in the blue channel and two 1800 s exposures in the red channel at an average airmass of 1.45, and observed the G2 V star HD 224 383 ($V = 8.8$) and the sdO spectrophotometric calibrator BD + 28 4211 (J. B. Oke 1990) for telluric and flux calibration, respectively. HeHgCd and HeNeArHg arc lamp exposures were used to wavelength calibrate the blue and red data, and flat-field lamp exposures were used for pixel response calibration. Data were reduced using the kastredux code[6] using standard settings. The spectrum of TOI-5916 has median SNRs of 16 at 5425 Å and 73 at 7350 Å. The spectrum of TOI-5292 A has median SNRs of 30 at 5425 Å and 95 at 7350 Å. The spectrum of TOI-5292 B has median SNRs of 2 at 5425 Å and 26 at 7350 Å.

3.2.4 *Magellan/MagE*

We observed TOI-3288 A and TOI-4666 on UTC 2022 Oct 6 with the Magellan Echellette spectrograph (MagE; J. L. Marshall et al. 2008) on the 6.5-m Magellan Baade Telescope. Conditions were clear, with seeing ranging from 0.7 to 1.5 arcsec over the night. We used the 0.7 arcsec × 10 arcsec slit, providing a resolving power of $\lambda/\Delta\lambda \approx 6000$ over 4000–9000 Å. For TOI-3288 A, we collected two 235-s exposures at an airmass of 1.4, and for TOI-4666, two 225-s exposures at an airmass of 1.0. For flux calibration, we observed the spectrophotometric standard Feige 110 (M. Hamuy et al. 1992, 1994), gathering two 375-s exposures at an airmass of 1.1. Wavelength calibration and pixel response corrections were performed using ThAr arcs, Xe flash lamps, bias, and incandescent lamp images. Since we did not observe a telluric standard, prominent atmospheric absorption features from O_2 and H_2O remain in the final spectra. Data reduction was carried out with PypeIt (J. X. Prochaska et al. 2020a, b; J. X. Prochaska et al. 2020c) using standard settings. The final spectra have median SNR of roughly 50 and 80 for TOI-3288 A and TOI-4666, respectively.

3.2.5 *SOAR/Goodman*

We observed TOI-5007 on UTC 2025 Apr 20 with the Goodman Spectrograph (J. C. Clemens, J. A. Crain & R. Anderson 2004) on the SOAR telescope through the AEON queue. Conditions were clear with 1.3 arcsec seeing. Using the red camera with the 400 lines mm^{-1} grating, a 1 arcsec slit, and 2 × 2 binning, we obtained four 300-s exposures spanning 0.5–0.9 µm at a resolving power of $R \approx 1000$. Standard sets of flat fields and arc lamps were collected immediately before and after the science sequence, and the spectrophotometric standard LTT 3218 was observed the same night for flux calibration. No telluric correction was applied. The data were reduced with PypeIt (J. X. Prochaska et al. 2020a, b; J. X. Prochaska et al. 2020c). The final spectrum has a median SNR of SNR ≈ 100.

3.2.6 *VLT/ESPRESSO*

We obtained between 4 and 6 high-resolution ($R \sim 140\,000$) spectra of all targets using the ESPRESSO spectrograph, mounted at the VLT of the ESO Paranal observatory (F. Pepe et al. 2021). The observations were carried out between UTC 2023 Dec and UTC 2025 Sep. The brighter TOI-3288 A, TOI-4666, and TOI-5007 were observed with an exposure time of 600 s, reaching on average an SNR of 7.1, 4.6, and 4.1 at 550 nm, respectively. The fainter stars TOI-5292 A and TOI-5916 were observed with exposure times of 1200 s and 900 s, reaching an average SNR of 5.3 and 2.3, respectively. All spectra were reduced by the ESO data reduction pipeline. Depending on the spectral type, we then used the M2 and K6 binary masks from the ESPRESSO pipeline[7] to generate cross-correlation functions (CCFs). These are derived in wide borders from −200 to 200 km s^{-1} at a resolution of 0.5 km s^{-1} for each spectral order and combined, weighted by the noise of each order. We used them to exclude any double-lined binaries and to derive a initial guess of the stellar RV. We then derived precise RVs of all targets, by fitting a double gaussian function introduced in D. Sebastian et al. (2024). This function includes the presence of side-lobes in CCFs of M-dwarfs. Here we only use a 40 km s^{-1} wide part of the CCF, centred at the expected RV of the star. We use these RVs in our global fit in Section 5, they are also reported in the Appendix, Tables E1–E5. Compared to the RVs, derived internally by the ESPRESSO pipeline, this additional step does not only allow us to measure or exclude any potential double-lined systems, it also does not require the knowledge of the stellar systemic velocity prior the derivation of the CCF. We compared RVs derived by both methods for our targets, but find no statistically significant difference.

3.2.7 *Magellan/PFS*

We observed TOI-5007 with the Planet Finder Spectrograph (PFS; J. D. Crane, S. A. Shectman & R. P. Butler 2006; J. D. Crane et al. 2008, 2010) on the 6.5 m Magellan II (Clay) telescope at Las Campanas Observatory. Between UTC 2023 Apr 8 and 2024 Jul 26 we

---

[6] https://github.com/aburgasser/kastredux.

[7] The ESPRESSO pipeline has been publicly released on https://www.eso.org.

obtained 7 visits, each consisting of three exposures of 1200 seconds, in 3 × 3 CCD binning mode with a 0.3 arcsec slit. This data was taken with the iodine gas absorption cell in the light path, which imprints a dense forest of molecular lines (A. P. Hatzes 2019) between 5000 and 6200 Å. We also obtained one template spectrum without the iodine cell consisting of six exposures of 1200 seconds. The RVs were derived following the methodology of R. P. Butler et al. (1996). As noted by J. D. Hartman et al. (2015) and G. Á. Bakos et al. (2020), due to the faintness of the target, and the optical region for the iodine region, the formal errors on the PFS RVs are likely underestimated. The final PFS RVs are included in E5 and as a machine readable table with the manuscript.

4 HOST CHARACTERIZATION

In this section, we combine spectroscopic, photometric and astrometric data with archival imagining to characterize the host stars. We begin with a search for line-of-sight or bound companions that could be blended in our photometry. We then determine physical parameters from spectroscopic analysis, scaling relations and spectral energy distribution (SED) analysis. Finally, we estimate kinematic ages for the stars in our sample. Adopted stellar parameters can be found in Table 1.

4.1 Archival imaging

In order to check for possible blends between our target star and bound or background objects, we query the *Gaia* DR3 Archive (Gaia Collaboration 2022) and investigate archival images for the systems discussed in this paper. All archival images can be found in Fig. C1.

For TOI-3288 A, we used data from the POSS-II/DSS (R. L. Minkowski & G. O. Abell 1963) in the infrared filter taken in 1991 and in the red filter in 1995, as well as SSO in $I + z$ taken in 2022, thus spanning 31 yr. The target has shifted 0.651 arcsec from 1991 to 2022, due to its proper motion of 21 mas yr^{-1} (Gaia Collaboration 2022). We find that there is a star very close to our target (*Gaia* DR3 6685431748040148992, TIC 1924436362, projected separation of 2.16 arcsec) with matching parallaxes and proper motions and a delta magnitude of 3.0 in the G band. M. Mugrauer, J. Rück & K.-U. Michel (2023) reports this star to be bound to TIC 79920467; therefore, TOI-3288 is a wide binary. Our ground-based photometric instruments are unable to separate the two components, so our observations in redder bands are partially diluted. However, the 1 arcsec aperture fibre of ESPRESSO confirmed the planet host to be TOI-3288 A.

For TOI-4666, we used data taken in the blue filter of POSS-II/DSS in 1977, its red filter in 1991, and the $I + z$ filter of SSO in 2023. The target has shifted by 1.06 arcsec in 46 yr, due to its proper motion of 23 mas yr^{-1}. No background objects are detected at the current position of the star.

For TOI-5007, we used data taken in the infrared filter of POSS-II/DSS in 1979, its red filter in 1992, and the *Sloan-i'* filter of SSO in 2023. The target has shifted by 1.52 arcsec in 44 yr, due to its proper motion of 33 mas yr^{-1}. The nearby field of TOI-5007 is crowded, and we find that there is a line-of-sight blended star (TIC 1116679820) at a projected separation of 1.85 arcsec. TIC 1 116 679 820 is 5 *TESS* magnitudes fainter than TOI-5007 and is therefore too faint to produce any significant contamination of our photometric or spectroscopic apertures.

For TOI-5292 A, we used data from the POSS-I/DSS (R. L. Minkowski & G. O. Abell 1963) taken in the red filter in 1953, the POSS-II/DSS infrared image taken in 1994 and the SPECULOOS-North image taken in the *Sloan-z* filter in 2024. The target has shifted by 0.78 arcsec in 71 yr due to its proper motion of 11 mas yr^{-1}. We once again find a nearby star with a similar astrometric solution (*Gaia* DR3 2610422028054589824, TIC 33397741, projected separation of 9.43 arcsec) which is 2.6 mag fainter in the G band. We use `CoMover` (J. Gagné et al. 2021), a Bayesian framework to determine the probability that stars are co-moving objects, and find the probability of these stars being a comoving pair is 99.99 per cent, and therefore determine TOI-5292 to be a wide binary. Given the larger projected separation of these stars, we are able to exclude the flux of the companion in our ground-based photometry.

For TOI-5916, we use images taken in 1953 (POSS-I/DSS, red filter), 1994 (POSS-II/DSS, infrared) and 2022 (SPECULOOS-North, *Sloan-g'* filter). The target has shifted by 1.86 arcsec in 69 yr due to its proper motion of 27 mas yr^{-1}, and no background objects are detected at the current position of the star.

4.2 Spectroscopic characterization

The SpeX spectra of TOI-5292 A and TOI-5916 are shown in Fig. 2. Comparison with single-star standards from the IRTF Spectral Library (M. C. Cushing, J. T. Rayner & W. D. Vacca 2005; J. T. Rayner, M. C. Cushing & W. D. Vacca 2009) using the SpeX Prism Library Analysis Toolkit (SPLAT; A. J. Burgasser & Splat Development Team 2017) indicates the best matches to the M0.5 V standard HD 209290 and the M1 V standard HD 42581, and we adopt near-infrared spectral types of M0.5 ±0.5 and M1.0 ±0.5 for TOI-5292 A and TOI-5916, respectively. From the K-band Na I and Ca I features and the H_2O–K2 index (B. Rojas-Ayala et al. 2012), we estimate iron enrichments of $[Fe/H] = +0.33 \pm 0.14$ for TOI-5292 A and $[Fe/H] = +0.09 \pm 0.14$ for TOI-5916, based on the A. W. Mann et al. (2013) relation. The SpeX spectrum of TOI-5292 B, the companion to TOI-5292 A, allows us to assign a spectral type of M3.5±0.5, but it does not have sufficient SNR for a metallicity estimate.

The TripleSpec4.1 spectra of TOI-3288 A, TOI-4666, and TOI-5007 are shown in Fig. 3. For TOI-3288 A and TOI-5007, we find the best matches to the M1.5 V standard HD 36395 and the M0 V standard HD 19305, respectively, and adopt NIR spectral types of M1.5±0.5 and M0±0.5. For TOI-4666, the best match is the K7 V standard HD 201092, but the next closest match is to the M0 V standard because the IRTF Spectral Library does not include K8 or K9 standards. Given this, we adopt an NIR spectral type of K8±1. Using the A. W. Mann et al. (2013) relation, we estimate [Fe/H] values of $+0.65 \pm 0.12$, $+0.79 \pm 0.14$, and $+0.43 \pm 0.12$ for TOI-3288 A, TOI-4666, and TOI-5007, respectively. Importantly, the metallicity estimates of TOI-3288 A and TOI-4666 lie outside the calibrated range of this relation ($-1.04 < [Fe/H] < +0.56$) and should be treated with caution.

The optical spectra of TOI-3288 A, TOI-4666, TOI-5007, TOI-5292 A, TOI-5292 B, and TOI-5916 are shown in Fig. 4. All of the spectra show spectral slopes and absorption features consistent with early mid-M dwarfs (M0–M2), with TOI-5292 B best matched to the M4 dwarf SDSS spectral template from J. J. Bochanski et al. (2007). These classifications were confirmed using index-based methods described in I. N. Reid, S. L. Hawley & J. E. Gizis (1995); J. E. Gizis (1997); and S. Lépine, R. M. Rich & M. M. Shara (2003). All of the spectra show weak absorption

Table 1. Stellar properties for all the systems considered in this work.

	TOI-3288 A	**TOI-4666**	**TOI-5007**	**TOI-5292 A**	**TOI-5916**
Designation					
TIC[1]	79 920 467	165 202 476	424 196 109	33 397 739	305 506 996
GAIA DR3[2]	6 685 431 748 042 347 776	4 855 422 771 071 903 232	5 833 386 583 912 265 728	2 610 422 023 759 160 576	1 741 429 438 313 012 608
2MASS[3]	J19482648-4301044	J03450956-3903470	J15441536-6102284	J22565337-0807108	J21411189 + 0935570
Photometric magnitudes					
TESS (mag)[1]	13.296 ±0.009	13.327 ±0.008	13.637 ±0.007	14.895 ±0.008	14.525 ±0.008
B (mag)[4]	16.485 ±0.119	16.746 ±0.084	17.718 ±0.169	18.329±0.162	18.286 ±0.165
V (mag)[4]	14.979 ±0.195	15.333 ±0.172	15.327±0.183	16.416 ±0.206	16.602±0.057
G (mag)[2]	14.234 ±0.001	14.391 ±0.001	14.652±0.001	15.909±0.001	15.693±0.001
J (mag)[3]	12.043 ±0.027	11.978 ±0.023	12.228±0.023	13.629 ±0.026	13.118±0.026
H (mag)[3]	11.421 ±0.034	11.289 ±0.022	11.52 ±0.022	12.955±0.022	12.444±0.03
Ks (mag)[3]	11.201 ±0.026	11.085 ±0.025	11.307±0.019	12.777±0.023	12.235 ±0.029
W1 (mag)[3]	11.035 ±0.022	10.999 ±0.023	11.229 ±0.023	12.693±0.024	12.091±0.023
W2 (mag)[3]	11.067 ±0.021	10.981 ±0.021	11.268±0.022	12.681±0.027	12.016±0.022
W3 (mag)[3]	10.924 ±0.134	10.844 ±0.061	11.16±0.254	>11.506	11.603±0.216
W4 (mag)[3]	>8.48	>9.512	>9.129	>8.537	>8.851
Astrometric properties					
Distance (pc)[5]	200.5 ±1.55	154.75 ±0.54	203.35 ±1.24	337.10 ±8.16	199.724 ±3.35
Parallax (mas)[2]	4.969 ±0.025	6.488 ±0.016	4.909 ±0.022	2.790 ±0.041	5.097 ±0.042
RA (J2000)[2]	19:48:26.48	03:45:09.57	15:44:15.33	22:56:53.37	21:41:11.88
DEC (J2000)[2]	−43:01:04.8	−39:03:47.45	−61:02:28.91	−08:07:11.09	+ 09:35:56.59
$\mu_{\rm RA}$[2]	−6.566 ±0.022	4.122 ±0.014	−13.515 ±0.026	−8.733 ±0.041	−8.816 ±0.039
$\mu_{\rm DEC}$[2]	−20.080 ±0.014	−22.135±0.019	−29.914 ±0.025	−6.862 ±0.039	−25.598 ±0.040
RUWE[2]	1.217	0.998	1.104	1.041	0.984
Adopted stellar parameters					
Opt. SpT	M0±0.5	M2±0.5	M1±0.5	M0±0.5	M2±0.5
NIR. SpT	M1.5±0.5	K8±1	M0±0.5	M0.5±0.5	M1±0.5
[Fe/H] (dex)	+0.65 ± 0.12	+0.79 ± 0.14	+0.43 ± 0.12	+0.33 ± 0.14	+0.09 ± 0.14
$R_\star$ (R$_\odot$)	0.672 ± 0.020	0.585 ± 0.018	0.656 ± 0.019	0.611 ± 0.019	0.480 ± 0.015
$M_\star$ (M$_\odot$)	0.643 ± 0.014	0.576 ± 0.012	0.632 ± 0.013	0.596 ± 0.013	0.477 ± 0.011
T$_{\rm eff}$ (K)	4072 ± 80	3793 ± 80	3793 ± 80	3919 ± 80	3613 ± 80
$\log g_\star$ (cgs)	4.592 ± 0.028	4.664 ± 0.028	4.604 ± 0.027	4.642 ± 0.029	4.755 ± 0.029
$L_\star$ (L$_\odot$)	0.1117 ± 0.0110	0.0638 ± 0.0066	0.0803 ± 0.0082	0.0792 ± 0.0081	0.0353 ± 0.0038
Age (Gyr)	5 ± 2	3^{+3}_{-2}	4 ± 2	5 ± 2	5 ± 2
U (kms^{-1})	25.54 ± 0.02	10.27 ± 0.03	$-14.54^{+0.08}_{-0.07}$	15.83 ± 0.25	$18.55^{+0.16}_{-0.14}$
V (kms^{-1})	$-21.70^{+0.08}_{-0.10}$	$-14.63^{+0.02}_{-0.04}$	$-24.16^{+0.09}_{-0.11}$	$-9.44^{+0.07}_{-0.10}$	$-15.85^{+0.11}_{-0.10}$
W (kms^{-1})	$-11.93^{+0.03}_{-0.02}$	−3.45 ± 0.02	$-15.20^{+0.05}_{-0.08}$	$9.62^{+0.04}_{-0.06}$	$-6.63^{+0.05}_{-0.07}$
SED fit					
$R_\star$ (R$_\odot$)	0.664 ± 0.020	0.577 ± 0.019	0.647 ± 0.019	0.595 ± 0.021	0.475 ± 0.018
$M_\star$ (M$_\odot$)	0.672 ± 0.028	0.598 ± 0.024	0.663 ± 0.024	0.615 ± 0.026	0.501 ± 0.026
$T_{\rm eff}$ (K)	4054 ± 62	3786 ± 59	3947 ± 73	3896 ± 61	3609 ± 66
$\log g_\star$ (cgs)	4.622 ± 0.025	4.692 ± 0.025	4.638 ± 0.024	4.678 ± 0.025	4.783 ± 0.026
$L_\star$ (L$_\odot$)	0.1073 ± 0.0046	0.0616 ± 0.0018	0.0911 ± 0.0051	0.0735 ± 0.0033	0.0345 ± 0.0015
[Fe/H] (dex)	+0.26 ± 0.20	+0.28 ± 0.12	+0.398 ± 0.096	+0.25 ± 0.14	+0.26 ± 0.14
$\rho_\star$ (g cm^{-3})	3.24 ± 0.27	4.38 ± 0.38	3.46 ± 0.28	4.12 ± 0.37	6.56 ± 0.61
A_v (mag)	0.137 ± 0.083	0.024 ± 0.018	0.23 ± 0.15	0.057 ± 0.046	0.088 ± 0.071

Sources: 1: K. G. Stassun et al. (2019); 2: Gaia Collaboration (2022); 3: R. M. Cutri et al. (2003); 4: N. Zacharias et al. (2013); 5: C. A. L. Bailer-Jones et al. (2021).

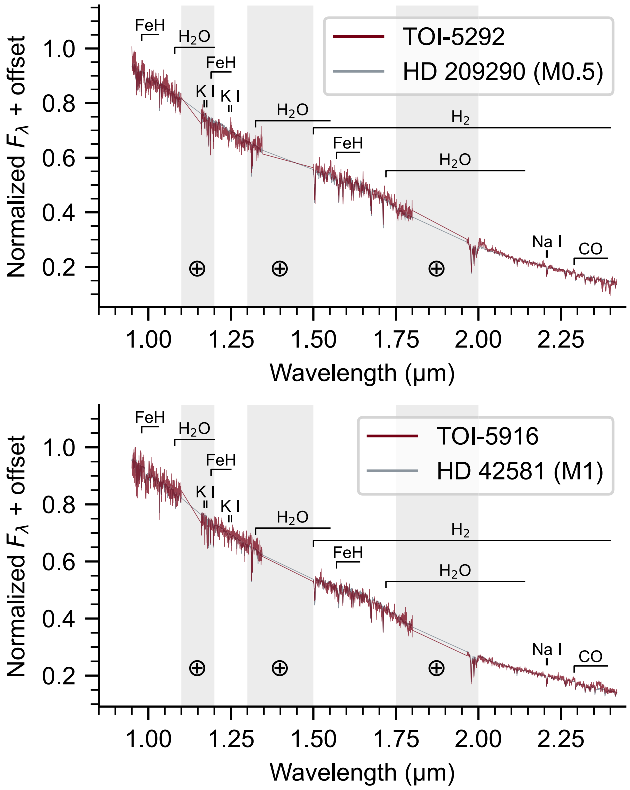

Figure 2. SpeX SXD spectra of TOI-5292 A (top) and TOI-5916 (bottom). The target spectra (red) are shown along with the closest spectral standard (grey). Spectral features of late-type stars are highlighted, and regions of strong tellurics are shaded.

features of H I, with the exception of TOI-4666 which exhibits emission in both Hβ (equivalent width EW $= -0.74\pm0.05$ Å) and H α (EW $= -0.59\pm0.03$ Å), the latter indicating a relative H α luminosity of $\log(L_{\mathrm{H}\,\alpha}/L_{\mathrm{bol}}) = -4.51 \pm 0.05$ using the χ factor relation of S. T. Douglas et al. (2014). Magnetic emission in an M2 dwarf indicates an activity age $\lesssim$1.2 Gyr (A. A. West et al. 2008), although there is no evidence of Li I absorption at 6708 Å ruling out an age less than $\sim$ 30 Myr. Metallicity indices for all of the sources are measured to be $\zeta \gtrsim 1$ indicating solar to slightly supersolar metallicities ($0 \lesssim$ [Fe/H] $\lesssim +0.5$).

We additionally used the empirical relations of A. W. Mann et al. (2015, 2019) to derive masses, radii, effective temperatures, surface gravities, and luminosities for TOI-3288 A, TOI-4666, TOI-5007, TOI-5292 A, and TOI-5916. These relations use 2MASS K_s magnitudes (M. F. Skrutskie et al. 2006) and *Gaia* DR3 parallaxes and BR–RP colours (Gaia Collaboration 2023). [Fe/H] measurements may optimally be used, but given the need for additional scrutiny of some of the [Fe/H] estimates reported here, we opted not to include any in the empirical calibrations.

We adopt the resulting stellar parameters in our analysis and present them in Table 1.

4.3 Spectral energy distribution

As an additional step to check our inferred stellar parameters, we used the publicly available exoplanet fitting suite EXOFASTv2 (J. Eastman 2017; J. D. Eastman et al. 2019), which employs a differential evolution Markov chain Monte Carlo (DE-MCMC) method to jointly fit stellar and exoplanetary parameters. We simultaneously fit the stellar SED while incorporating the MESA Isochrones and Stellar Tracks (MIST; (B. Paxton et al. 2015). To sample the stellar SED, we used available broad-band apparent magnitudes (see Fig. D1), obtained using MKSED, a programme distributed with EXOFASTv2 that automatically queries the most trusted photometric catalogs. Gaussian priors were imposed on the Gaia DR3 parallax (Gaia Collaboration 2020), which was corrected following the prescription of L. Lindegren et al. (2021). An upper limit on the V-band extinction, A_V, was set based on reddening maps (D. J. Schlegel, D. P. Finkbeiner & M. Davis 1998; E. F. Schlafly & D. P. Finkbeiner 2011).

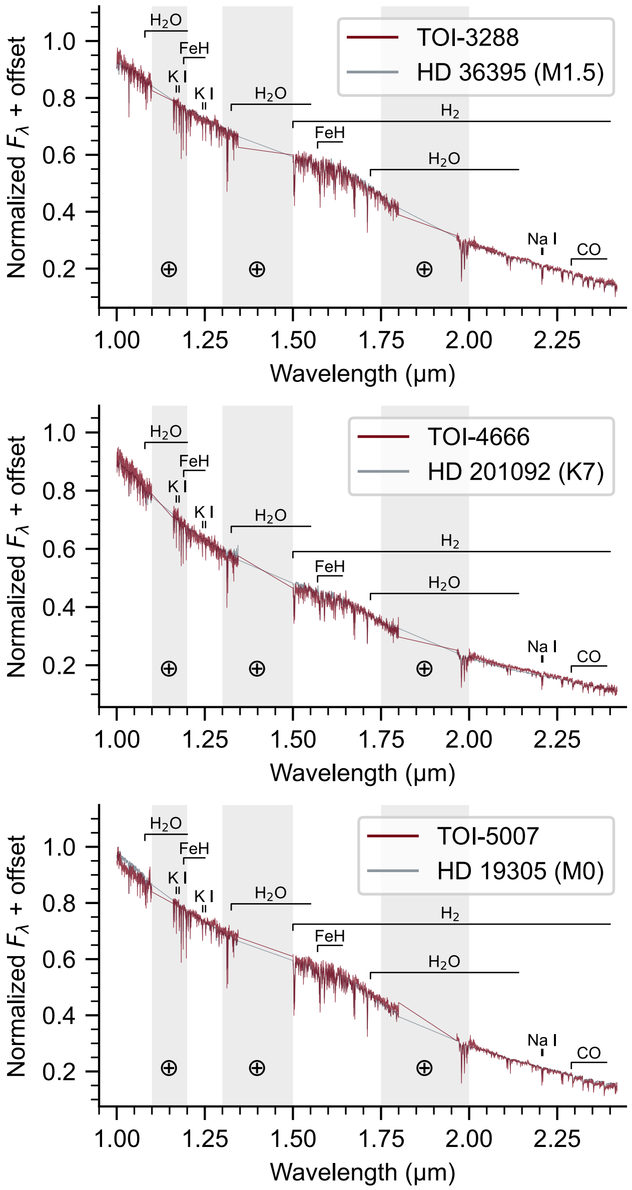

Figure 3. TripleSpec4.1 spectra of TOI-3288 A (top), TOI-4666 (middle), and TOI-5007 (bottom). The figure elements are the same as those of Fig. 2. Note that the TripleSpec4.1 spectra of the targets (red) have higher spectral resolving power than the SpeX spectra of the standards ($R$$\sim$3500versus $R$$\sim$2000).

The results of the SED fitting are summarized in Table 1 for comparison and the resulting fits are presented in Fig. D1.

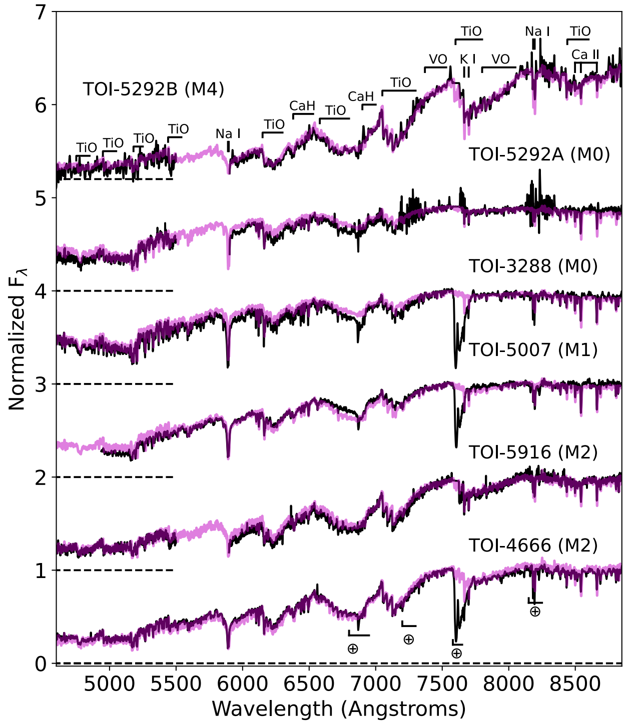

Figure 4. Optical spectra of (from bottom to top) TOI-4666 (MagE), TOI-5916 (Kast), TOI-5007 (Goodman), TOI-3288 A (MagE), and TOI-5292 A and B (Kast; black lines) compared to their best-fitting spectral standards from J. J. Bochanski et al. (2007, magneta lines). All spectra are normalized at 7400 Å and offset by constants (dashed lines). Key spectral features are labeled, including uncorrected telluric absorption (⊕) in the MagE and Goodman spectra.

4.4 Age Estimation

Following the methods outlined in A. J. Burgasser & E. E. Mamajek (2017); L. Delrez et al. (2022); G. Dransfield et al. (2023), we estimate the ages of the stars in our sample by comparing their *UVW* velocities and metallicities to a selection of stars in the GALAH DR3 catalogue (S. Buder et al. 2021). The comparison samples have ages estimated from isochrone fittings using Bayesian Stellar Parameter Estimation (BSTEP; S. Sharma et al. 2018) and metallicities measured from high resolution spectroscopy.

We compute the Galactic heliocentric orbital velocities *UVW* for each star in our sample from their ESPRESSO RVs and their five-parameter *Gaia* DR3 astrometric solutions, for which we correct the parallax for the noted zero-point offset following L. Lindegren et al. (2021). The adopted Galactic parameters are a solar position of $(\mathrm{X}_\odot, \mathrm{Y}_\odot, \mathrm{Z}_\odot) = (8.2, 0, 0.0208)$ kpc, a Local Standard of Rest velocity of 240 km s^{-1}, and a solar peculiar motion with respect to the LSR of $(\mathrm{U}_\odot, \mathrm{V}_\odot, \mathrm{W}_\odot) = (11.1, 12.24, 7.25)$ km s^{-1} (R. Schönrich, J. Binney & W. Dehnen 2010; J. Bovy 2015; M. Bennett & J. Bovy 2019; Gravity Collaboration et al. 2019). The resulting *UVW* are reported in Table 1. The five stars show kinematics typical of the Galactic thin disc, which hosts relatively young, near-solar-metallicity stars like the Sun. Their supersolar metallicities are consistent with this classification and suggest ages younger than ~ 4 Gyr, in line with Galactic chemical enrichment models (E. Spitoni et al. 2019).

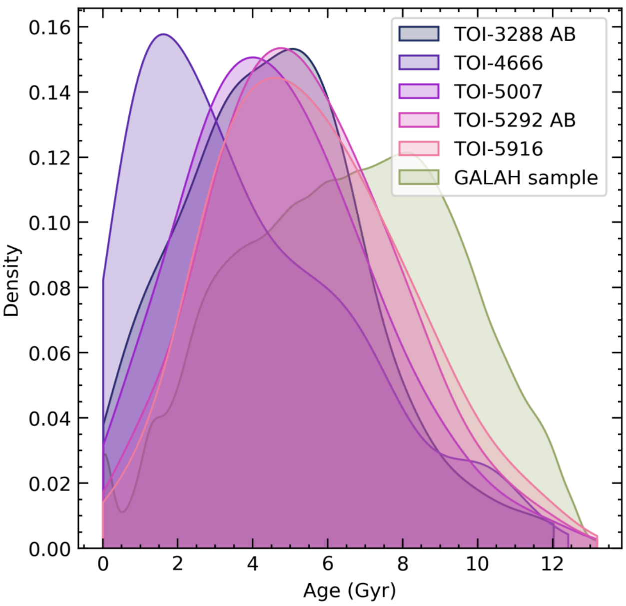

Figure 5. Distribution of ages for matched stars in the GALAH DR3 catalogue for each star in our sample in their respective colours. In the background in green we show the full GALAH sample for comparison.

We select a matching sample from GALAH DR3 for each of our stars, with distances ≤ 250 pc, *UVW* velocities agreeing to within 15 km s^{-1}, and metallicities agreeing to within 0.3 dex.

For TOI-3288 A, we find 369 matched stars with a median age of $4.53^{+1.60}_{-1.69}$ Gyr. For TOI-4666 we widened the constraint on matching velocity to 20 km s^{-1} as only 129 matching stars were found initially. With the constrained thus relaxed, we found 277 matching stars with a median age of $3.10^{+2.61}_{-1.66}$ Gyr. For TOI-5007 we find 6121 matching stars with a median age of $4.48^{+1.88}_{-1.60}$ Gyr. For TOI-5292 A, we find 2124 matching stars with a median age of $5.18^{+1.84}_{-1.60}$ Gyr. Finally for TOI-5916 we find 11 674 matching stars with a median age of $5.31^{+1.97}_{-1.70}$ Gyr.

We present the estimated ages in Table 1 and the age distributions for matched stars as well as the full GALAH sample in Fig. 5. Given the challenges associated with estimated precise stellar ages, we report slightly larger uncertainties of 2 Gyr for all our stars, except TOI-4666 where we increase this to 3 Gyr.

5 GLOBAL ANALYSIS

We use ALLESFITTER (M. N. Günther & T. Daylan 2019, 2021, and references therein) to jointly model all available photometry and RV data sets, following the procedures detailed in G. Dransfield et al. (2022, 2023) and described here in brief.

We adopt the signal parameters reported by SPOC (J. M. Jenkins et al. 2016; D. A. Caldwell et al. 2020) as uniform priors and the stellar parameters reported in Table 1 as normal priors. For the uniform priors, we use a prior width of 1day for period and transit midtime, and bounds of ±10 per cent for all other fitted parameters. Additionally, we use PYLDTK (H. Parviainen & S. Aigrain 2015) and the Phoenix stellar atmosphere models (T. O. Husser et al. 2013) to calculate quadratic limb darkening parameters which we adopt as normal priors after reparametrizing them in the (D. M. Kipping 2013) parametrization.

We fit for all transit parameters ($R_\mathrm{p}/R_\star$, $(R_\star + R_\mathrm{p})/a$, cos i, T_0, and P) and allow the eccentricity to vary as a free parameter,

Table 2. Fitted and derived parameters from our global fits.

			Fitted parameters		
	TOI-3288 Ab	**TOI-4666 b**	**TOI-5007**	**TOI-5292 Ab**	**TOI-5916 b**
$R_b/R_\star$	$0.16701^{+0.00090}_{-0.00080}$	0.19653 ± 0.00042	$0.1547^{+0.0017}_{-0.0015}$	$0.1897^{+0.0024}_{-0.0023}$	0.2169 ± 0.0016
$(R_\star + R_b)/a_b$	$0.1592^{+0.0047}_{-0.0030}$	0.09610 ± 0.0010	0.1149 ± 0.0030	$0.1211^{+0.0046}_{-0.0039}$	$0.1032^{+0.013}_{-0.0059}$
$\cos i_b$	0.0175 ± -0.011	$0.0036^{+0.0034}_{-0.0024}$	$0.0895^{+0.0047}_{-0.0048}$	0.020 ± 0.012	$0.0140^{+0.010}_{-0.0081}$
$T_{0;b}$(BJD)	2460343.9069 ± 0.0001	$2460265.13619 \pm 0.00007$	2460068.8110 ± -0.0001	2460551.1467 ± 0.0002	2460255.6055 ± 0.0002
P_b(d)	1.4338647 ± 0.0000003	2.9089165 ± 0.0000007	2.543371 ± 0.000001	2.021910 ± 0.000003	2.367128 ± 0.000001
$K_b(\mathrm{km\,s^{-1}})$	$0.433^{+0.016}_{-0.017}$	0.103 ± 0.013	$0.1314^{+0.0057}_{-0.0056}$	0.3115 ± 0.010	$0.173^{+0.037}_{-0.019}$
$\sqrt{e_b}\cos\omega_b$	$-0.03^{+0.11}_{-0.10}$	$-0.01^{+0.15}_{-0.11}$	$-0.023^{+0.081}_{-0.084}$	$-0.107^{+0.080}_{-0.060}$	$-0.06^{+0.23}_{-0.20}$
$\sqrt{e_b}\sin\omega_b$	$0.01^{+0.14}_{-0.12}$	-0.008 ± 0.065	$0.260^{+0.047}_{-0.071}$	$-0.115^{+0.13}_{-0.091}$	$0.17^{+0.20}_{-0.24}$
			Derived parameters		
R_b ($\mathrm{R_{jup}}$)	1.092 ± 0.033	1.118 ± 0.035	0.988 ± 0.031	$1.128^{+0.039}_{-0.037}$	$1.013^{+0.032}_{-0.033}$
M_b ($\mathrm{M_{jup}}$)	$1.687^{+0.114}_{-0.109}$	$0.489^{+0.067}_{-0.066}$	$0.664^{+0.043}_{-0.042}$	$1.299^{+0.081}_{-0.074}$	$0.713^{+0.241}_{-0.114}$
a_b (AU)	$0.02285^{+0.00089}_{-0.00092}$	0.0340 ± 0.0011	0.0307 ± 0.0012	0.0279 ± -0.0013	$0.0262^{+0.0021}_{-0.0029}$
$a_\mathrm{b}/R_\star$	$7.33^{+0.14}_{-0.21}$	12.45 ± 0.13	$10.05^{+0.27}_{-0.26}$	$9.82^{+0.33}_{-0.35}$	$11.79^{+0.71}_{-1.30}$
i_b (deg)	89.00 ± -0.61	$89.79^{+0.14}_{-0.19}$	$84.86^{+0.28}_{-0.27}$	$88.87^{+0.69}_{-0.72}$	$89.20^{+0.47}_{-0.58}$
e_b	$0.021^{+0.026}_{-0.015}$	$0.023^{+0.033}_{-0.016}$	$0.074^{+0.026}_{-0.030}$	$0.034^{+0.024}_{-0.020}$	$0.090^{+0.114}_{-0.062}$
w_b (deg)	174^{+91}_{-108}	183^{+50}_{-49}	95^{+19}_{-18}	227^{+29}_{-53}	114^{+89}_{-54}
$b_\mathrm{tra;b}$	$0.128^{+0.074}_{-0.077}$	$0.045^{+0.042}_{-0.030}$	0.836 ± 0.008	$0.199^{+0.116}_{-0.119}$	$0.158^{+0.088}_{-0.091}$
$T_\mathrm{tot;b}$ (h)	$1.737^{+0.008}_{-0.007}$	2.137 ± 0.004	$1.442^{+0.015}_{-0.014}$	$1.884^{+0.023}_{-0.019}$	$1.774^{+0.015}_{-0.013}$
$T_\mathrm{full;b}$ (h)	$1.229^{+0.007}_{-0.009}$	1.432 ± -0.004	$0.249^{+0.071}_{-0.091}$	$1.257^{+0.017}_{-0.029}$	$1.125^{+0.015}_{-0.016}$
ρ_b ($\mathrm{g\,cm^{-3}}$)	$1.60^{+0.23}_{-0.20}$	$0.43^{+0.08}_{-0.07}$	$0.85^{+0.12}_{-0.11}$	$1.12^{+0.16}_{-0.14}$	$0.86^{+0.31}_{-0.18}$
$T_\mathrm{eq;b}$ (K)	973^{+24}_{-23}	695 ± 15	774 ± 19	809^{+22}_{-21}	683^{+43}_{-29}
S ($\mathrm{S_\oplus}$)	213.8 ± 27.2	55.6 ± 6.8	85.3 ± 12.2	102.0 ± 14.2	51.7 ± 12.6

parametrized as $\sqrt{e_\mathrm{b}}\cos\omega_\mathrm{b}$ and $\sqrt{e_\mathrm{b}}\sin\omega_\mathrm{b}$ (following A. H. M. J. Triaud et al. 2011). We expect all orbits to be circular given the short orbital periods (e.g. T. Guillot et al. 1996); therefore, any robustly detected eccentricity could indicate an additional perturbing body in the system.

Baseline trends in the photometry are modeled using ALLESFITTER's 'hybrid spline' functionality, and the 'hybrid offset' is used for the RVs. Finally, we fit a jitter term which is added in quadrature to the RV errors and an 'error scaling' term to account for white noise in the photometric data. We use the nested sampling algorithm DYNESTY (J. S. Speagle 2020) in all our fits. The results of our global fits can all be found in Table 2, with additional fitted and derived parameters presented for individual systems in Appendix F.

In the case of TOI-5007 b, we made use of an additional free parameter to account for the dilution of the *TESS* signal by neighbouring stars. Using the SAP flux, we used a uniform prior between −1 and 1.

6 RESULTS

In this section, we summarize the results for each system, highlighting key parameters and standout features.

6.1 TOI-3288 Ab

TOI-3288 Ab is a $1.092 \pm 0.033\mathrm{R_{jup}}$ planet with a mass of $1.687^{+0.114}_{-0.109}\mathrm{M_{jup}}$. As such, it is the densest planet in our sample. Our model finds an eccentricity consistent with zero at the 2σ level ($0.021^{+0.026}_{-0.015}$). We calculate the tidal circularization timescale for TOI-3288 Ab following T. Guillot et al. (1996), taking Jupiter's values for the tidal dissipation factor, $Q \sim 10^5$, and the planet's primordial rotation rate, $\omega_\mathrm{p} \sim 1.7 \times 10^{-4}\mathrm{s}^{-1}$. We also use the value of tidal dissipation factor, $Q \sim 10^{6.5}$, reported in B. Jackson, R. Greenberg & R. Barnes (2008) to account for the difficulty in accurately deriving this quantity. We find that the planet would have circularized in $0.05 - 1.5$Gyr, which is consistent with our finding of a circular orbit given our system age estimation. In Fig. 6, we present the transits used in our fits along with best-fitting models, as well as the RV points from ESPRESSO.

As described above, TOI-3288 A is in a close binary system and most of our ground-based photometry is contaminated by the secondary. Inspection of the radial PSF plots showed that the companion is not detected in our bluest band, $Sloan - g'$. We therefore fixed the dilution parameter in our fits to zero for this band, and set a uniform prior of $\mathcal{U}(0, 0.1)$ in remaining bands. This prior was informed by calculating the maximum dilution expected in our reddest bands based on the fluxes of both components measured by *Gaia* in the G_{rp} band. The fitted dilutions for each band are presented in Table F1, and the result of adding these parameters is that the planet radius increased by ∼ 10 per cent compared with the initial model without dilution.

The planetary radius measurement could still be under or overestimated, as several of the transits of TOI-3288 Ab show spot crossings. In fact, of the systems presented in this work, TOI-3288 A is the most consistently spotty host. Comprehensive analysis of the spot parameters (latitudes, longitudes, and contrasts, and sizes) is beyond the scope of this work, and will be presented in a

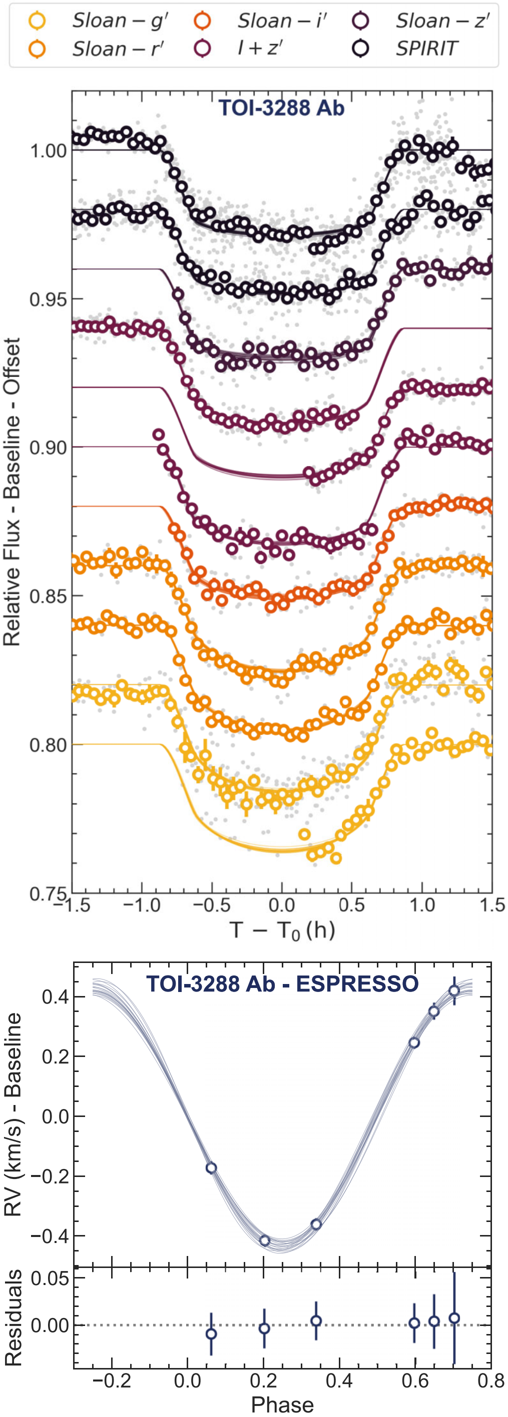

Figure 6. Models for TOI-3288 Ab obtained from a joint photometry + RV fit. *Top:* Photometry of TOI-3288 Ab along with best-fitting models. Raw flux is plotted in grey and 15-min binned flux in white circles outlined in colours to indicate the wavelength band the observation was taken in. Transit models are corrected for by subtracting the baseline. All transits have a relative offset applied for plotting. The model lines are 20 random draws from the posterior transit model. Where multiple transits were observed by an instrument in the same filter, these are phase-folded. *Bottom:* Phase-folded RVs of TOI-3288 A from ESPRESSO. Model lines are 20 random draws from posterior RV model. RV models is corrected by subtracting the baseline model.

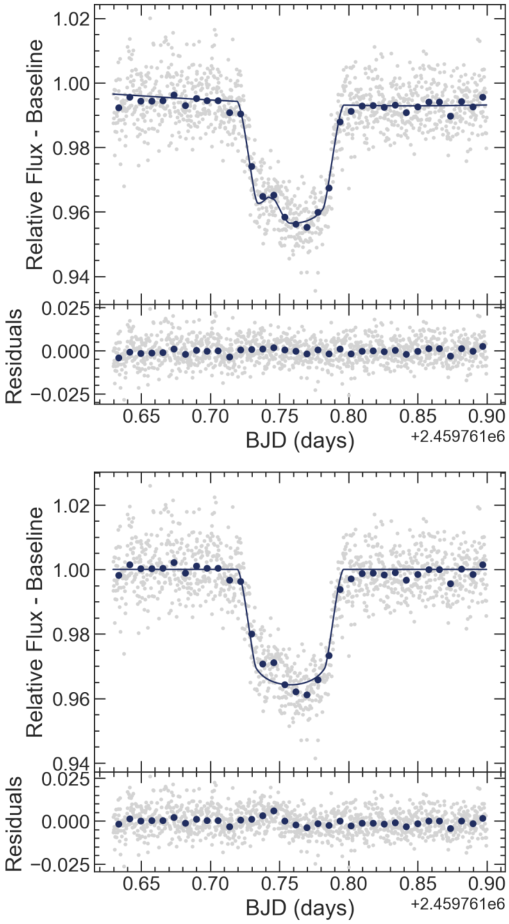

Figure 7. Comparison of fits with and without a physical spot model for one transit epoch of TOI-3288 Ab. The upper figure is the alternative hypothesis which includes a single starspot, while the bottom figure is the null hypothesis.

future paper by F. Davoudi (in preparation). However, to illustrate the potential effects of spot crossings on the inferred planetary radius, we select one transit epoch observed with SSO/Callisto in zYJ that has a clear spot crossing event. We fit a model including ALLESFITTER's physical spot model, and compare it to the null hypothesis, which consists of a transit model with no starspot. We compare the Bayesian evidence for the models by calculating the Bayes Factor, $\Delta \ln Z$. In both cases, we fit circular models with fixed T_0, P, and limb darkening coefficients. We present both fitted models in Fig. 7.

We find that the model including one spot is preferred with a Bayes Factor $\Delta \ln Z = 23.9$. In the interpretation of J. S. Miller & R. P. S. Stone (1994), $\Delta \ln Z > 5$ is considered decisive evidence. The radius derived from the null is $0.03 R_\oplus$ smaller (2.5 per cent) than the alternative model radius. This is less than a 1σ difference, which indicates that the scatter introduced by spot crossings in our transits is well accounted for in our uncertainties. The effect of spot crossings is also mitigated by phase folding repeated observations taken with the same instrument using the same filter.

We note that as we have not used any of the *TESS* data in our analysis, our results are completely independent of those presented in Y. G. C. Frensch et al. (2025).

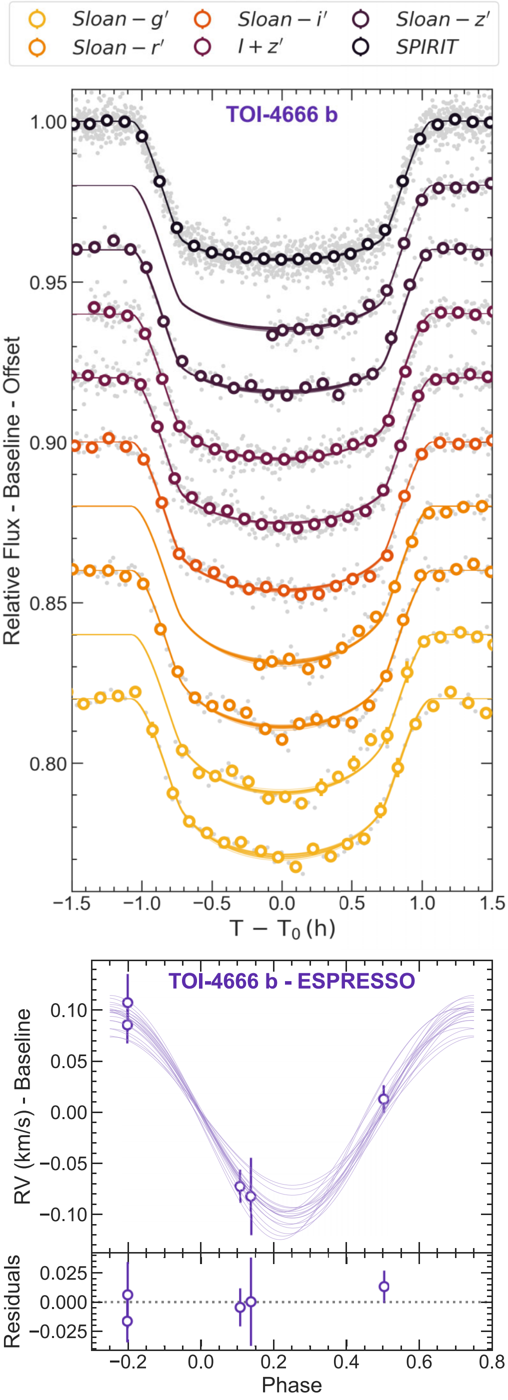

Figure 8. Same as Fig. 6 but for TOI-4666.

6.2 TOI-4666 b

TOI-4666b is a $1.118 \pm 0.035\mathrm{R_{jup}}$ planet with a mass of $0.489^{+0.067}_{-0.066}\mathrm{M_{jup}}$. It the lowest density planet in our sample ($\rho_b = 0.43^{+0.08}_{-0.07}\,\mathrm{g\,cm^{-3}}$), with a density ~ 60 per cent that of Saturn ($0.69\,\mathrm{g\,cm^{-3}}$). Like TOI-3288 Ab, there are spot crossings evident on many of the individual transits, leading to some additional scatter in the data. All transits and RV points used in this can be found in Fig. 8.

The eccentricity derived from our fit is once again consistent with zero; however, as can be seen in the bottom panel of Fig. 8, the sampling of the orbit is uneven. In the case of TOI-4666 b, further RV points would be beneficial to confirm the low eccentricity in light of the low system age revealed in Section 3.2. Calculating the tidal circularization time-scale as above, using the same values of Q, we find a circularization time-scale for TOI-4666 b of 0.2–6.5 Gyr. Therefore, without more data we cannot be certain whether the orbit is circular or not.

As with TOI-3288 Ab, the results presented here are completely independent of those presented in Frensch et al. (in preparation).

6.3 TOI-5007 b

TOI-5007 b is a $0.991 \pm 0.030\mathrm{R_{jup}}$ planet with a mass of $0.684^{+0.051}_{-0.047}\mathrm{M_{jup}}$. In Fig. 9 we present the transits used in our fits along with best-fitting models, as well the RV points from ESPRESSO and PFS.

For this planet, our fit finds a small but non-zero eccentricity at the 3σ level of $e_b = 0.100^{+0.037}_{-0.038}$. As above we calculate the tidal circularization time-scale and find it to be $\tau \approx 1.7 - 5.4$Gyr. Given our system age estimation, it is possible that this planet could still be undergoing tidal circularization.

However, an alternative explanation for the detected eccentricity could be an additional body in the system which continues to force the eccentricity. We searched for additional signals in the RV residuals using a Generalized Lomb–Scargle periodogram (M. Zechmeister & M. Kürster 2009) and do not find any additional periodicities. We searched for additional transiting planets in all the available *TESS* sectors using the TLS (M. Hippke & R. Heller 2019). Given the large gap in time and the different cadences between the *TESS* Sectors 12 (1800 s), 39 (600 s), and 65 (120 s), we applied the transit search algorithm to the individual Sectors. The period grid extends from the Roche limit to 15 d, which corresponds to half a Sector to include at least two transit events. For Sector 12, we performed the search on both the GSFC-ELEANOR-LITE (B. P. Powell et al. 2022) raw and corrected fluxes. For the raw flux, we made use of the `wōtan` package (M. Hippke et al. 2019) to remove long-term systematic trends, with window sizes between 0.1 and 0.5. The signal of TOI-5007 b is recovered at a low SNR of 6.4 in the best-case scenario, with only a couple of in-transit data points. No other signals over the nominal threshold for candidate detection of SNR = 5 were found. We performed a similar analysis for Sectors 39 and 65, using both the raw and corrected fluxes to search for hints of additional transit events. In both cases, the signal of planet b was recovered with SNR of 6.5 and 14.4, respectively. Correspondingly to Sector 12, no convincing additional periodic signals were found.

Further scrutiny of the RV data and models in Fig. 9 reveals that the orbit is not evenly sampled. In particular, there is limited sampling between phases −0.2 and 0.2, and the scatter around phase 0 is smaller than the rest of the PFS data. All 20 models drawn from the posterior in this figure pass through these data at phase 0.0, so this is likely driving the fit. As described in Section 3.2.7 there are 21 PFS spectra collected across seven nights, effectively producing seven distinct measurements.

To test the impact of intra-night variation on the derived eccentricity, we average the three nightly spectra. While the loss of time resolution is unlikely to have an impact, the risk of averaging the measurements is artificially shrinking the uncertainties. To be as conservative as possible, we calculate an unweighted mean of the three nightly RVs and estimated the uncertainty as the root-mean-square (RMS) of the individual uncertainties. We rerun our global fit of the data with the averaged PFS data and find that the

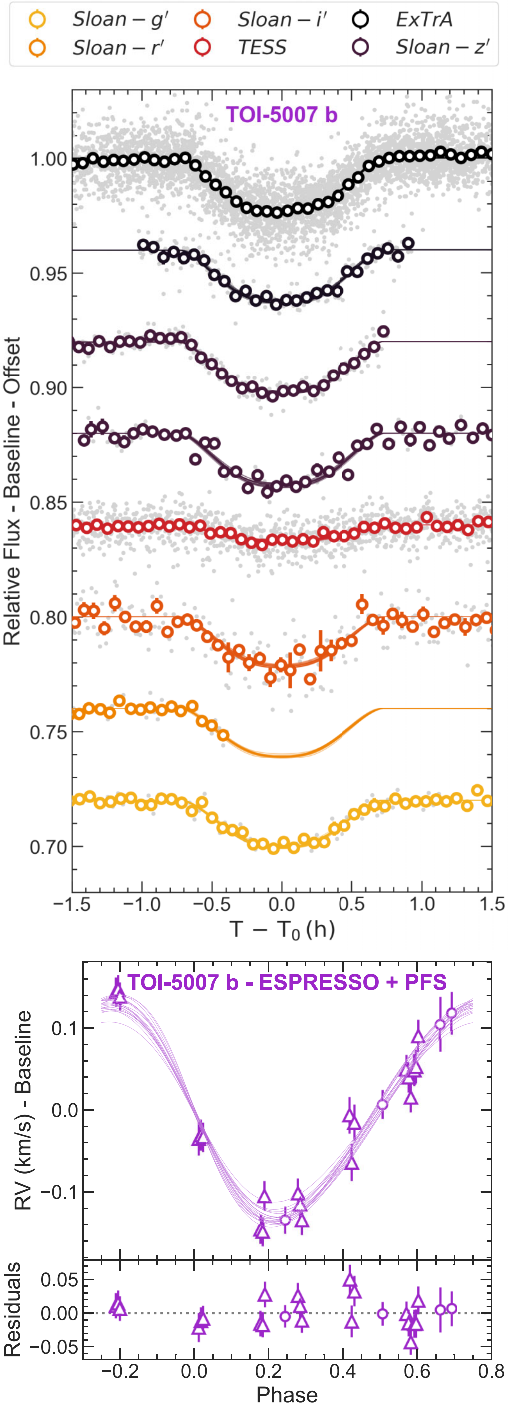

Figure 9. Same as Fig. 6 but for TOI-5007. The *TESS* SAP flux appears shallower than the ground-based data because of the dilution of the signal by neighbouring stars. In the bottom panel we plot the PFS RV points as triangles and the ESPRESSO points as circles.

eccentricity reduces to $0.080^{+0.034}_{-0.041}$, which is consistent with zero at the 2σ level.

Given the uncertainty associated with this planet's eccentricity, we report in Table 2 the value derived from modelling all the available data, and emphasize that more RV points sampling the full orbital phase will be crucial to conclusively rule in or out an eccentric orbit for this planet.

TOI-5007 b has the highest impact parameter in our sample, with a configuration that is almost grazing. In fact, the large number of transits collected by ExTrA with their near-infrared capabilities was critical in constraining the shape of the transit and therefore the planetary radius.

We did not include a dilution parameter for the ground-based photometry as the blended non-bound companion is > 5 magnitudes fainter and is not detected. We tested the global analysis using both the PDCSAP flux of *TESS*, which is corrected for the dilution of the signal in the pipeline aperture, and the SAP flux which has no corrections. The SAP flux combined to a free dilution parameter provided a better fit to the data than the PDCSAP flux where the transit seemed too deep compared to the model. The PDCSAP flux then seems over-corrected for crowding with a dilution of 77 per cent, while the fitted value was 72±2 per cent as defined in ALLESFITTER.

6.4 TOI-5292 Ab

TOI-5292 Ab is a $1.128^{+0.039}_{-0.037}\mathrm{R_{jup}}$ planet with a mass of $1.299^{+0.081}_{-0.074}\mathrm{M_{jup}}$, making it the second highest density planet in our sample ($\rho_\mathrm{b} = 1.12^{+0.16}_{-0.14}\mathrm{g\,cm^{-3}}$) and the closest to Jupiter ($1.33\mathrm{g\,cm^{-3}}$). In Fig. 10, we present the transits used in our fits along with best-fitting models, as well the RV points from ESPRESSO.

The eccentricity of the planet is found to be consistent with zero at the 2σ level, and as can be seen in the lower panel of Fig. 10 the orbit is very evenly sampled. As before, we calculate τ which gives a range 0.14 − 4.6 Gyr suggesting that tidal circularization would indeed be complete given the system age of $5.23^{+1.77}_{-1.65}$Gyr.

As the bound companion is well separated in the photometry, we do not include any dilution in our model.

6.5 TOI-5916 b

TOI-5916 b is a $1.013^{+0.032}_{-0.033}\mathrm{R_{jup}}$ planet with a mass of $0.713^{+0.241}_{-0.114}\mathrm{M_{jup}}$. In Fig. 11, we present the transits used in our fits along with best-fitting models, as well the RV points from ESPRESSO.

Our fit finds an eccentricity of $e = 0.090^{+0.114}_{-0.062}$, which is the second highest we measure, but is still consistent with zero at the 2σ level. The eccentricity cannot be well constrained by our fit as the RV sampling is not even enough in the orbit. However, with a calculated tidal circularization time-scale of < 3.9Gyr, we would not expect this planet to be eccentric.

7 DISCUSSION

In this section, we contextualize the five new MANGOS systems presented in this work. In Fig. 12, we present the sample of giant transiting planets as queried from the NASA Exoplanet Archive[8] (J. L. Christiansen et al. 2025). In the background, we show giants orbiting FGK stars, and in the foreground we present the planets discovered so far that meet the MANGOS program criteria ($P < 7$ d, $R_\mathrm{p} > 7\mathrm{R}_\oplus$, $T_\mathrm{eff} < 4000$ K). The five planets presented in this work are shown in their respective colours as well as contours indicating the densities of Jupiter and Saturn.

TOI-4666 b is the only planet in our sample with a density lower than Saturn, sharing the parameter space with 11 other

---

[8] Accessed on UTC 2025 Sep 25

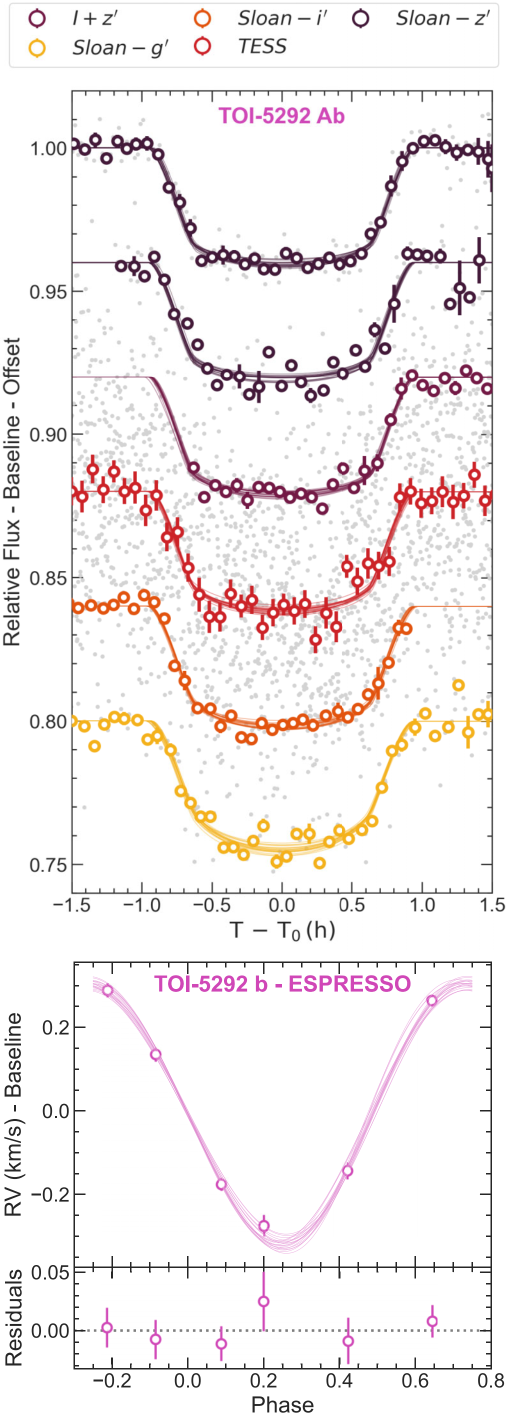

Figure 10. Same as Fig. 6 but for TOI-5292 A.

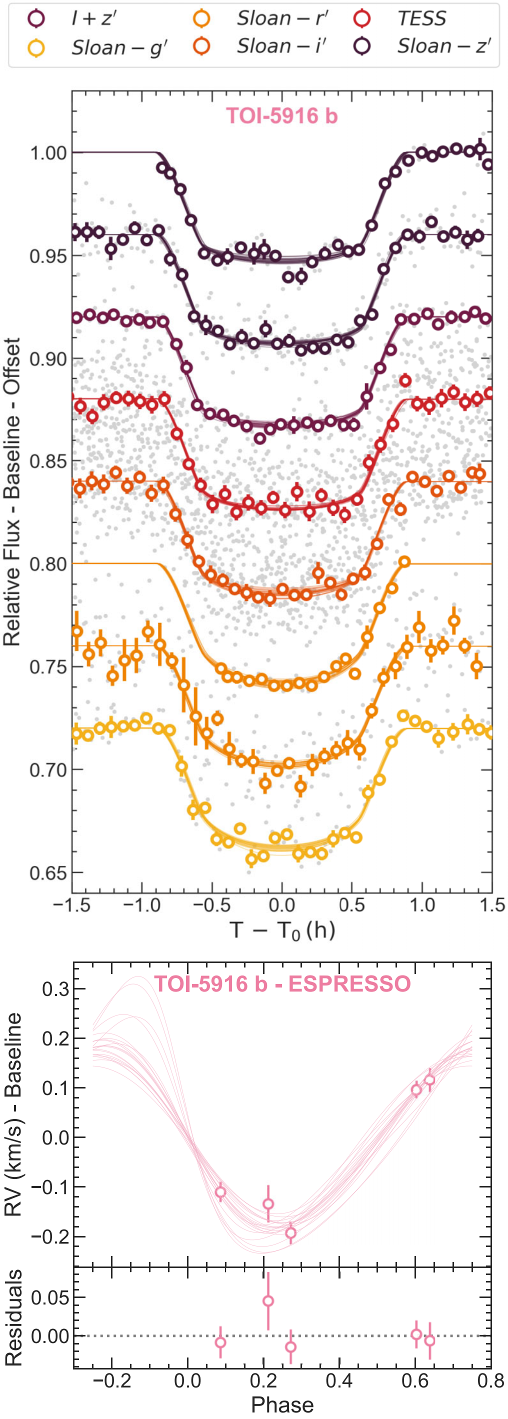

Figure 11. Same as Fig. 6 but for TOI-5916.

MANGOS-type planets, the most similar being TOI-519 b (H. Parviainen et al. 2021b; J. D. Hartman et al. 2023) and TOI-5293 Ab (C. I. Cañas et al. 2023). Conversely, one of the planets in our sample (TOI-3288 Ab) is slightly denser than Jupiter, similar to seven other giants orbiting low-mass stars. The remaining three have densities intermediate between the solar system gas giants. The planets are very similar to each other, and also to the recently discovered TOI-7149 b (S. Kanodia et al. 2025). However we note that the mass of TOI-5916 b is the least constrained in our sample, as described above.

7.1 Could these MANGOS have formed by core accretion?

One of the motivations for searching for giant planets orbiting M dwarfs is the challenge they pose to our understanding of planet formation (e.g. E. M. Bryant et al. 2023; S. Kanodia et al. 2024). In the current paradigm, giant planets on short orbits form via

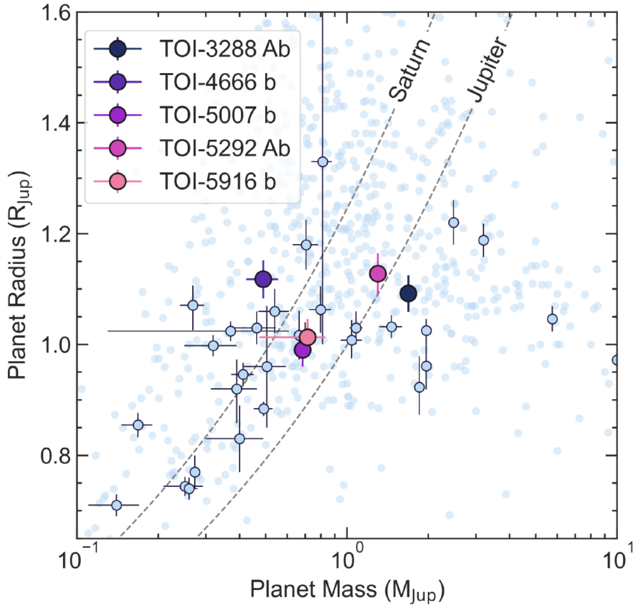

Figure 12. Mass–radius of transiting giant exoplanets with measured masses, as queried from the NASA Exoplanet Archive. In the background in light blue are giant planets orbiting FGK stars. Light blue planets with black edges and error bars are MANGOS-type planets: giants orbiting M dwarfs with periods < 7 d. The five planets presented in this work are shown in their respective colours. The two dashed lines show the density contours at Saturn and Jupiter's densities.

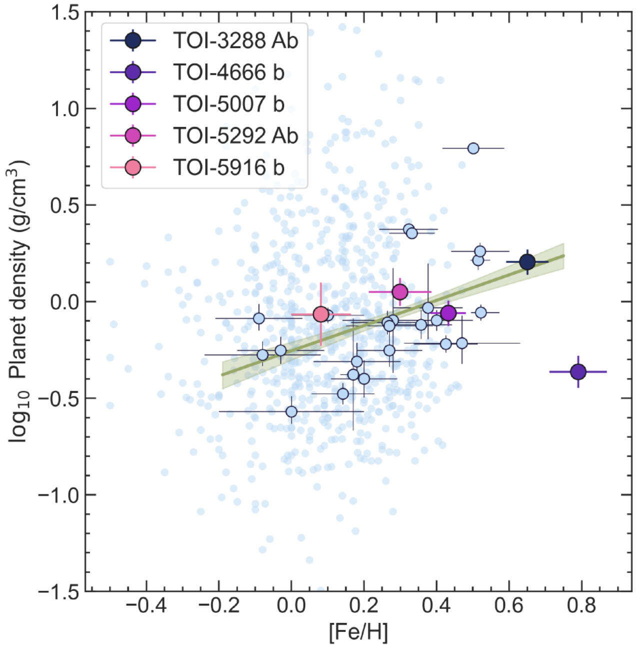

Figure 13. Planet density versus host star metallicity. All planets shown in this figure are transiting planets with measured masses as queried from the NASA Exoplanet Archive. In the background in light blue are giant planets orbiting FGK stars. Light blue planets with black edges and error bars are MANGOS-type planets: giants orbiting M dwarfs with periods < 7 d. The five planets presented in this work are shown in their respective colours. We show the best fit regression line from our analysis in green, as well as the 68 per cent confidence interval.

core accretion, where small solids (pebbles or planetesimals) will gradually come together to form a planetary embryo (J. B. Pollack et al. 1996; B. Liu & J. Ji 2020). Once these embryos become massive enough, runaway gas accretion can kick in, allowing large envelopes of H/He gas to be acquired (S. Ida & D. N. C. Lin 2005).

The challenge to this model when it comes to MANGOS is that on average the mass of the protoplanetary disc scales with the mass of the host star (e.g. S. M. Andrews et al. 2013; M. Ansdell et al. 2017), which means that formation of close-in giant planets becomes increasingly difficult with decreasing stellar mass due to lower availability of solids. A further challenge is that the runaway gas accretion phase has to complete before the gas in the disc dissipates, but the time-scale for these cores to form is significantly longer around M stars than around FGK stars (G. Laughlin et al. 2004).

Two host stars in our sample have masses $M_{\star} > 0.6\,\mathrm{M}_{\odot}$: TOI-3288 A and TOI-5007. The closest host mass considered by R. Burn et al. (2021) in their population synthesis is $0.7\,\mathrm{M}_{\odot}$, and at this mass the formation of giant planets can easily be reconciled with core accretion. In fact, their simulations indicate that 9 per cent of stars in this mass range would host giant planets. TOI-4666 and TOI-5292 A have masses $< 0.6\,\mathrm{M}_{\odot}$ making them more comparable to the $0.5\mathrm{M}_{\odot}$ hosts in the simulations. Here R. Burn et al. (2021) find that only 2 per cent of systems host giant planets due to the decreased efficiency of core accretion.

TOI-5916 has a mass of $0.47 \pm 0.01\mathrm{M}_{\odot}$ - the lowest in our sample. For masses $< 0.5\mathrm{M}_{\odot}$ no giant planets were formed in the population synthesis of R. Burn et al. (2021). However, TOI-5916 b is the 11th giant planet discovered orbiting a star in this mass range. Assuming a maximum disc-to-star mass ratio of 0.6 per cent (S. M. Andrews et al. 2013) and a dust-to-gas mass ratio of 1 per cent, we find that the maximum amount of dust available in TOI-5916's protoplanetary disc is $\sim 9.6\mathrm{M}_{\oplus}$. Given that a core of $\sim 10\mathrm{M}_{\oplus}$ is needed to trigger runaway gas accretion (C. Mordasini et al. 2008), this implies that 100 per cent of available solids in the disc would be used in the formation of this core.

Therefore, in order for TOI-5916 b to have formed via core accretion, we would require a higher star-to-disc mass ratio, a very dust rich disc and highly efficient core formation.

7.2 The impact of host metallicity on planet bulk density

In Fig. 13, we show $\log_{10}$ planet density versus host star metallicity for all planets in the NASA Exoplanet Archive that meet MANGOS programme criteria. In the background we plot all other giant transiting planets, and we overplot the five new MANGOS presented in this work.

For this discussion on stellar metallicity, we note that the difficulty of accurately measuring host metallicities of M dwarfs is well documented in the literature (e.g. S. Lindgren & U. Heiter 2017). The challenges lie in the vast amount of molecular lines present in M-dwarf spectra, as well as the wide variety of approaches used to extract stellar metallicity. V. M. Passegger et al. (2022) found that different methods can lead to discrepancies of up to 0.3 dex. The values for our host stars used in this analysis are those presented in Table 1 which were extracted from near-infrared spectra (see Section 3). The values for other MANGOS-type planets are those presented in the NASA Exoplanet Archive Composite Data table, and they were extracted using various methods. We therefore emphasize that caution is needed when looking at relationships involving the metallicity of low-mass host stars.

With the exception of TOI-4666 b[9], we find that the planets in this work are consistent with the existing population of MANGOS-type planets on Fig. 13. The planet-metallicity relation is well studied (e.g. J. A. Johnson et al. 2010; D. P. Thorngren et al. 2016), and recent works have investigated whether this extends to low-mass stars (T. Gan et al. 2025a).

We investigate a potential correlation between host metallicity and planet bulk density for MANGOS planets. First we calculate the Pearson correlation coefficient to check for a statistically significant correlation, finding values of $r = 0.558$, $p = 0.00202$, where a p value <0.05 is considered statistically significant.

We then use a Monte Carlo linear regression to account for the measurement uncertainties in both host metallicity and planet bulk density. As the density uncertainties are asymmetric, we select the larger of the two values in each case. For each system, we draw 10 000 random values of $\log_{10}$ density and metallicity from Gaussian distributions centred on their measured values, fitting a straight line to each simulated dataset. In this way we build up posterior distributions for the slope and intercept allowing us to extract best-fitting values. We measure a slope of 0.654 ± 0.139 and an intercept of -0.253 ± 0.048, which gives the following relationship between host metallicity and planet bulk density:

$$\rho = 0.558 \times 10^{0.654\times[\mathrm{Fe/H}]}. \quad (1)$$

We overplot the median and 68 per cent confidence intervals for this relationship on Fig. 13.

D. P. Thorngren et al. (2016) searched for a link between planetary heavy element mass and host star metallicity; despite previous studies finding such a link with smaller sample sizes (e.g. N. Miller & J. J. Fortney 2011), this result was not replicated. More recently J. K. Teske et al. (2019) carried out a similar study with homogenously determined metallicities and also found no link.

Planet bulk density is a good proxy for planet heavy element mass, as can be seen from the data presented by D. P. Thorngren et al. (2016). Given our result, it is possible that such a correlation between heavy element mass and stellar metallicity exists for giant planets in short orbits around low-mass stars. Given that MANGOS planets are cooler on average, we might expect them to track the initial metallicity of the protoplanetary disc more securely. Such an investigation is beyond the scope of this paper, but it presents an exciting avenue of investigation for future studies.

7.3 The possible eccentricity of TOI-5007 b

Our global analysis of TOI-5007 b revealed a small but non-zero eccentricity. From our calculation of tidal circularization timescales and our measured kinematic age of the star, we were unable to confirm whether this planet is expected to have circularized yet. However, two other MANGOS-type planets with 3σ detected eccentricities exist.

TOI-2379 b (E. M. Bryant et al. 2024) is a super-Jupiter with a robustly detected eccentricity of 0.3420 ± 0.0039, and the authors calculate a maximum tidal circularization time-scale of $\tau = 16.6$Gyr. This is significantly longer than the system age they determine from isochrone fitting (13.8 ± 4.1Gyr). TOI-6330 b is another super-Jupiter (A. Hotnisky et al. 2025) with a measured eccentricity of 0.34 ± 0.01; once again the authors derive a value for τ that is longer than the system age of 7.6 ± 4.9Gyr. Both of these planets have masses significantly larger than Jupiter ($5.76 \pm 0.2\mathrm{M_{jup}}$ and $10.0 \pm 0.32\mathrm{M_{jup}}$ respectively), while TOI-5007 b has a more modest mass of $0.684^{+0.051}_{-0.047}\mathrm{M_{jup}}$. Their higher masses could be indicative of different formation pathways such as gravitational instability, given the need for significantly more solids in the protoplanetary disc (A. Mercer & D. Stamatellos 2020). Therefore the eccentricity of TOI-5007 b might have a different origin.

It would be beneficial to collect further RV points for this system in order to confirm the eccentricity and place better constraints on additional planets in the system. Thus far, no MANGOS-type planets have been found to reside in multiplanet systems, so small eccentricities provide an exciting avenue for exploration. Given that warm Jupiters around FGK stars very often have planetary siblings (C. Huang, Y. Wu & A. H. M. J. Triaud 2016), understanding whether this is true or not of MANGOS will help reveal similarities between these different flavours of giant planets.

7.4 How might we further characterize these MANGOS?

Given the exceptionally deep transits produced by MANGOS planets and the ease with which masses can be constrained, they appear at first glance to be an ideal population for atmospheric investigations via transmission spectroscopy. The transmission spectroscopy metric (TSM, E. M. R. Kempton et al. 2018) is a convenient way to quantify the suitability of an exoplanet for investigations of this kind. We calculate the TSM for all the planets in our sample, and find modest values of between 21–53 for all planets except TOI-4666 b, which has a TSM of 116 due to its low density. These values are largely consistent with the rest of the MANGOS-type planets, for which we calculate TSMs of between 3 and 350. For context, E. M. R. Kempton et al. (2018) suggest a cut-off value of 96 to pursue observations of this kind for planets in the radius regime of MANGOS.

Nevertheless, temperate giant planets are expected to have interesting molecular features such as C, N and O bearing species (J. J. Fortney et al. 2020) which would allow determination of C/O and N/O ratios if detected. Both of these quantities contain critical information about the formation environment and location in the disc of a planet (e.g. K. I. Öberg, R. Murray-Clay & E. A. Bergin 2011; N. Madhusudhan et al. 2017; D. Turrini et al. 2021; P. Mollière et al. 2022; C. Walsh 2025). Given the enduring mysteries surrounding the origin of giant planets in tight orbits around M dwarfs, atmospheric investigations are a crucial piece of the puzzle, and well worth pursuing.

The difficulty comes in dealing with the stellar contamination likely to be present in the observed spectra (e.g. B. V. Rackham, D. Apai & M. S. Giampapa 2018, 2019). Indeed, first results from the GEMS (Giant Exoplanets around M dwarf Stars) programme on *JWST* (C. I. Cañas et al. 2025) revealed significant stellar contamination, leading to degeneracies in the inferred abundances of H_2O. Despite these challenges, they made robust detections of CH_4 and H_2S.

Given that we detect persistent spot crossings on at least two planets presented in this work, including TOI-4666 b which has the largest TSM, more work needs to be done to develop mitigation techniques for stellar contamination (e.g. A. R. Iyer & M. R. Line 2020; B. V. Rackham et al. 2023; B. V. Rackham & J. de Wit 2024).

Spots are not always a hindrance, though. Another crucial piece of the formation history puzzle can come from measuring

---

[9] We exclude TOI-4666 from this analysis given the very high metallicity we derived, and the fact it may be young.

the sky-projected angle between a planet's orbit and the stellar spin, known as the stellar obliquity. While stellar obliquity measurements are often obtained by observing a RV anomaly during transit (A. H. M. J. Triaud 2018; S. H. Albrecht, R. I. Dawson & J. N. Winn 2022), they can also be constrained by mapping out stellar rotation in systems with persistent star spots (e.g. R. Sanchis-Ojeda, J. N. Winn & D. C. Fabrycky 2013; A. Valio & A. Araújo 2022; F. Biagiotti et al. 2024; S. Sagynbayeva et al. 2025). Several MANGOS targets are amenable to these kinds of investigations, providing another path to revealing the formation history of these planets.

Whether a system is aligned or misaligned can provide insights into its migration history – which, together with constraints on the orbital eccentricity, may offer an avenue to distinguish between the hot Jupiter formation scenarios of *in situ* formation, disc migration, or high-eccentricity migration (R. I. Dawson & J. A. Johnson 2018; M. Rice et al. 2022). Such M-dwarf-hosted planets may be particularly useful for distinguishing between models for the tidal interactions that sculpt the stellar obliquity distribution for hot Jupiters, as M dwarfs lack radiative zones that are required for certain proposed tidal damping mechanisms to operate (J. J. Zanazzi, J. Dewberry & E. Chiang 2024).

8 CONCLUSIONS

In this work we have presented our project called MANGOS: **M** dwarfs **A**ccompanied by close-i**N** **G**iant **O**rbiters with **S**PECULOOS, a programme designed to discover giant planets, BDs and M dwarfs orbiting low-mass stars, with the goal of better understanding the various formation environments around M dwarfs and calibrating the mass–radius relation at the bottom of the main sequence.

We have presented the discovery and confirmation of five new MANGOS planets: TOI-3288 Ab ($R_\mathrm{b} = 1.092 \pm 0.033\mathrm{R_{jup}}$, $M_\mathrm{b} = 1.687^{+0.114}_{-0.109}\mathrm{M_{jup}}$), TOI-4666 b ($R_\mathrm{b} = 1.118 \pm 0.035\mathrm{R_{jup}}$, $M_\mathrm{b} = 0.489^{+0.067}_{-0.066}\mathrm{M_{jup}}$), TOI-5007 b ($R_\mathrm{b} = 0.991 \pm 0.030\mathrm{R_{jup}}$), $M_\mathrm{b} = 0.684{-}0.047^{+0.051}\mathrm{M_{jup}}$, TOI-5292 Ab ($R_\mathrm{b} = 1.128^{+0.039}_{-0.037}\mathrm{R_{jup}}$, $M_\mathrm{b} = 1.299^{+0.081}_{-0.074}\mathrm{M_{jup}}$), and TOI-5916 b ($R_\mathrm{b} = 1.013^{+0.032}_{-0.033}\mathrm{R_{jup}}$, $M_\mathrm{b} = 0.713^{+0.241}_{-0.114}\mathrm{M_{jup}}$). TOI-3288 Ab and TOI-4666 b show persistent spot crossings on their transits, making them amenable to characterization of their stellar obliquities. Our modelling of TOI-5007 b revealed a 3σ detection of an eccentric orbit ($e_\mathrm{b} = 0.100^{+0.037}_{-0.038}$), but further RV points are needed to confirm this detection and investigate if it is caused by an additional body in the system.

We find that all but one of the systems (TOI-5916) are consistent with formation via core accretion. TOI-5916 b could have formed via core accretion by invoking higher disc-to-star and gas-to-dust mass ratios, and very high core formation efficiencies.

We detect bound stellar companions for two stars in our sample (TOI-3288 A and TOI-5292 A), and in the case of TOI-5292 A we are able to characterize both components of the binary. Our spectroscopic characterization revealed high metallicities for several of our targets, which we interpret with caution. These measurements emphasize the challenge of acquiring robust metallicities for M dwarfs.

We also show that for MANGOS planets, there is a strong correlation between host star metallicity and planet bulk density. Again, this should be interpreted with caution, but it could be indicative of a relation between stellar metallicity and heavy element mass in planets.

Our work brings the total number of MANGOS-type planets to 35. Continued detection of new systems, and their follow-up characterization, will enable more robust measurements of occurrence rates and improve our understanding of how giant planets form in diverse stellar environments.

ACKNOWLEDGEMENTS

We thank the reviewer for their helpful comments which improved and clarified the manuscript. We also thank Philippe Thebault from the Paris Observatory for alerting us that TOI-3288AB was already a known binary reported by a previous work.

GD acknowledges funding from Magdalen College, Oxford. Funding for KB was provided by the European Union (ERC AdG SUBSTELLAR, GA 101054354). This material is based upon work supported by the National Aeronautics and Space Administration under Agreement No. 80NSSC21K0593 for the program 'Alien Earths'. The results reported herein benefited from collaborations and/or information exchange within NASA's Nexus for Exoplanet System Science (NExSS) research coordination network sponsored by NASA's Science Mission Directorate. This material is based upon work supported by the European Research Council (ERC) Synergy Grant under the European Union's Horizon 2020 research and innovation program (grant no. 101118581–project REVEAL). We acknowledge financial support from the Agencia Estatal de Investigación of the Ministerio de Ciencia e Innovación MCIN/AEI/10.13039/501100011033 and the ERDF 'A way of making Europe' through project PID2021-125627OB-C32, and from the Centre of Excellence 'Severo Ochoa' award to the Instituto de Astrofisica de Canarias. MG is F.R.S-FNRS Research Director. YGMC is partially supported by UNAM PAPIIT-IG101224 JDH and GAB acknowledge funding from NASA grant no. 80NSSC22K0315 EJ is F.R.S-FNRS Research Director. AS acknowledges support from the European Research Council Consolidator Grant funding scheme (project ASTEROCHRONOMETRY, G.A. n. 772293, http://www.asterochronometry.eu). Visiting Astronomer at the Infrared Telescope Facility, which is operated by the University of Hawaii under contract 80HQTR24DA010 with the National Aeronautics and Space Administration. Based in part on observations obtained at the Southern Astrophysical Research (SOAR) telescope, which is a joint project of the Ministério da Ciência, Tecnologia e Inovações (MCTI/LNA) do Brasil, the US National Science Foundation's NOIRLab, the University of North Carolina at Chapel Hill (UNC), and Michigan State University (MSU). The paper is based on observations made with the Kast spectrograph on the Shane 3m telescope at Lick Observatory. A major upgrade of the Kast spectrograph was made possible through generous gifts from the Heising-Simons Foundation and William and Marina Kast. We acknowledge that Lick Observatory sits on the unceded ancestral homelands of the Chochenyo and Tamyen Ohlone peoples, including the Alson and Socostac tribes, who were the original inhabitants of the area that includes Mt. Hamilton. J.d.W. and MIT gratefully acknowledge financial support from the Heising-Simons Foundation, Dr and Mrs Colin Masson and Dr Peter A. Gilman for Artemis, the first telescope of the SPECULOOS network situated in Tenerife, Spain. This work is partly supported by JSPS KAKENHI Grant Number JP24H00017, JP24K00689, and JSPS Bilateral Program Number JPJSBP120249910. This article is based on observations made with the MuSCAT2 instrument, developed by ABC, at Telescopio Carlos Sánchez operated on the island of Tenerife by the IAC in the Spanish Observatorio del Teide. The ULiege's contribution to

SPECULOOS has received funding from the European Research Council under the European Union's Seventh Framework Programme (FP/2007-2013) (grant agreement no. 336480/SPECULOOS), from the Balzan Prize and Francqui Foundations, from the Belgian Scientific Research Foundation (F.R.S.-FNRS; grant no. T.0109.20), from the University of Liege, and from the ARC grant for Concerted Research Actions financed by the Wallonia-Brussels Federation. The Cambridge contribution is supported by a grant from the Simons Foundation (PI Queloz, grant number 327127). JdW and MIT gratefully acknowledge financial support from the Heising-Simons Foundation, Dr and Mrs Colin Masson and Dr Peter A. Gilman for Artemis, the first telescope of the SPECULOOS network situated in Tenerife, Spain. The Bern contribution is supported by the Swiss National Science Foundation (PP00P2-163967, PP00P2-190080 and the National Centre for Competence in Research PlanetS). The Birmingham contribution to SPECULOOS has received fund from the European Research Council (ERC) under the European Union's Horizon 2020 research and innovation programme (grant agreement no. 803193/BEBOP), from the MERAC foundation, and from the Science and Technology Facilities Council (STFC; grant no. ST/S00193X/1) and from the ERC/UKRI Frontier Research Guarantee programme (EP/Z000327/1/CandY). TRAPPIST is funded by the Belgian Fund for Scientific Research (Fond National de la Recherche Scientifique, FNRS) under the grant PDR T.0120.21, with the participation of the Swiss National Science Fundation (SNF). TRAPPIST-North is funded by the University of Liège in collaboration with the Cadi Ayyad University of Marrakech. We acknowledge funding from the European Research Council under the ERC Grant Agreement no. 337591-ExTrA.

We acknowledge the use of public TESS data from pipelines at the TESS Science Office and at the TESS Science Processing Operations Center. Resources supporting this work were provided by the NASA High-End Computing (HEC) Program through the NASA Advanced Supercomputing (NAS) Division at Ames Research Center for the production of the SPOC data products.

This paper includes data gathered with the 6.5 m Magellan Telescopes located at Las Campanas Observatory, Chile.

DATA AVAILABILITY

TESS data products are available via the MAST portal at https://mast.stsci.edu/portal/Mashup/Clients/Mast/Portal.html. Follow-up photometry and high-resolution imaging data for TOIs are available on ExoFOP at https://exofop.ipac.caltech.edu/tess/. These data are freely accessible to ExoFOP members immediately and are publicly available following a 1-yr proprietary period. RVs are provided in tables in Appendix E of this manuscript.

REFERENCES

Albrecht S. H., Dawson R. I., Winn J. N., 2022, PASP, 134, 082001
Alibert Y., Mordasini C., Benz W., Winisdoerffer C., 2005, A&A, 434, 343
Andrews S. M., Rosenfeld K. A., Kraus A. L., Wilner D. J., 2013, ApJ, 771, 129
Ansdell M., Williams J. P., Manara C. F., Miotello A., Facchini S., van der Marel N., Testi L., van Dishoeck E. F., 2017, AJ, 153, 240
Bailer-Jones C. A. L., Rybizki J., Fouesneau M., Demleitner M., Andrae R., 2021, AJ, 161, 147
Bakos G. Á. et al., 2020, AJ, 159, 267
Baraffe I., Homeier D., Allard F., Chabrier G., 2015, A&A, 577, A42
Barkaoui K. et al., 2019, AJ, 157, 43
Barkaoui K. et al., 2024, A&A, 687, A264
Barkaoui K. et al., 2025a, A&A, 695, A281
Barkaoui K. et al., 2025b, A&A, 696, A44
Baruteau C. et al., 2014, in Beuther H., Klessen R. S., Dullemond C. P., Henning T., eds, Protostars and Planets VI. p. 667, preprint (arXiv:1312.4293)
Batygin K., Bodenheimer P. H., Laughlin G. P., 2016, ApJ, 829, 114
Bennett M., Bovy J., 2019, MNRAS, 482, 1417
Berger D. H. et al., 2006, ApJ, 644, 475
Biagiotti F. et al., 2024, A&A, 685, A131
Bochanski J. J., West A. A., Hawley S. L., Covey K. R., 2007, AJ, 133, 531
von Boetticher A. et al., 2019, A&A, 625, A150
Boley A. C., Granados Contreras A. P., Gladman B., 2016, ApJ, 817, L17
Bonfils X. et al., 2015, in Shaklan S., ed., Proc. SPIE Conf. Ser. Vol. 9605, Techniques and Instrumentation for Detection of Exoplanets VII. SPIE, Bellingham, p. 96051L
Boss A. P., 1997, Science, 276, 1836
Boss A. P., 2006, ApJ, 644, L79
Boss A. P., Kanodia S., 2023, ApJ, 956, 4
Bovy J., 2015, ApJS, 216, 29
Brown T. M. et al., 2013, PASP, 125, 1031
Bryant E. M., Bayliss D., Van Eylen V., 2023, MNRAS 3663–3681
Bryant E. M. et al., 2024, MNRAS, 533, 3893
Bryant E. M. et al., 2025, Nat. Astron., 9, 1031
Buder S. et al., 2021, MNRAS, 506, 150
Burdanov A., Delrez L., Gillon M., Jehin E., 2018, in Deeg H. J., Belmonte J. A., eds, Handbook of Exoplanets. Springer International Publishing AG, p. 130
Burdanov A. Y. et al., 2022, PASP, 134, 105001
Burgasser A. J., Mamajek E. E., 2017, ApJ, 845, 110
Burgasser A. J., Splat Development Team, 2017, in Astronomical Society of India Conference Series. p. 7, preprint (arXiv:1707.00062)
Burn R., Schlecker M., Mordasini C., Emsenhuber A., Alibert Y., Henning T., Klahr H., Benz W., 2021, A&A, 656, A72
Butler R. P., Marcy G. W., Williams E., McCarthy C., Dosanjh P., Vogt S. S., 1996, PASP, 108, 500
Cañas C. I. et al., 2022, AJ, 164, 50
Cañas C. I. et al., 2023, AJ, 166, 30
Cañas C. I. et al., 2025, preprint (arXiv:2502.06966)
Caldwell D. A. et al., 2020, Res. Notes Am. Astron. Soc., 4, 201
Casagrande L., Flynn C., Bessell M., 2008, MNRAS, 389, 585
Chabrier G., Johansen A., Janson M., Rafikov R., 2014, in Beuther H., Klessen R. S., Dullemond C. P., Henning T., eds, Protostars and Planets VI. p. 619, preprint (arXiv:1401.7559)
Christiansen J. L. et al., 2025, Planet. Sci. J., 6, 186
Clemens J. C., Crain J. A., Anderson R., 2004, in Moorwood A. F. M., Iye M., eds, Proc. SPIE Conf. Ser. Vol. 5492, Ground-based Instrumentation for Astronomy. SPIE, Bellingham, p. 331
Cointepas M. et al., 2021, A&A, 650, A145
Collins K. A., Kielkopf J. F., Stassun K. G., Hessman F. V., 2017, AJ, 153, 77
Crane J. D., Shectman S. A., Butler R. P., 2006, in McLean I. S., Iye M., eds, Proc. SPIE Conf. Ser. Vol. 6269, Ground-based and Airborne Instrumentation for Astronomy. SPIE, Bellingham, p. 626931
Crane J. D., Shectman S. A., Butler R. P., Thompson I. B., Burley G. S., 2008, in McLean I. S., Casali M. M., eds, Proc. SPIE Conf. Ser. Vol. 7014, Ground-based and Airborne Instrumentation for Astronomy II. SPIE, Bellingham, p. 701479
Crane J. D., Shectman S. A., Butler R. P., Thompson I. B., Birk C., Jones P., Burley G. S., 2010, in McLean I. S., Ramsay S. K., Takami H., eds, Proc. SPIE Conf. Ser. Vol. 7735, Ground-based and Airborne Instrumentation for Astronomy III. SPIE, Bellingham, p. 773553
Cushing M. C., Vacca W. D., Rayner J. T., 2004, PASP, 116, 362
Cushing M. C., Rayner J. T., Vacca W. D., 2005, ApJ, 623, 1115
Cutri R. M. et al., 2003, VizieR Online Data Catalog, p. II/246
Dawson R. I., Johnson J. A., 2018, ARA&A, 56, 175
Delamer M. et al., 2024, ApJ, 962, L22

Delrez L. et al., 2018, in Marshall H. K., Spyromilio J., eds, Proc. SPIE Conf. Ser. Vol. 10700, Ground-based and Airborne Telescopes VII. SPIE, Bellingham, p. 107001I
Delrez L. et al., 2022, A&A, 667, A59
Demory B. O. et al., 2020, A&A, 642, A49
Douglas S. T. et al., 2014, ApJ, 795, 161
Dransfield G. et al., 2022, MNRAS, 515, 1328
Dransfield G. et al., 2024, MNRAS 527 35–52
Eastman J., 2017, EXOFASTv2: Generalized publication-quality exoplanet modeling code, preprint (ascl:1710.003)
Eastman J. D. et al., 2019, preprint (arXiv:1907.09480)
Emsenhuber A., Mordasini C., Burn R., Alibert Y., Benz W., Asphaug E., 2021, A&A, 656, A70
Feiden G. A., Chaboyer B., 2013, in Pavlovski K., Tkachenko A., Torres G., eds, EAS Publications Series Vol. 64, EAS Publications Series. EDP, p. 127, preprint (arXiv:1310.8567)
Fortney J. J., Visscher C., Marley M. S., Hood C. E., Line M. R., Thorngren D. P., Freedman R. S., Lupu R., 2020, AJ, 160, 288
Frensch Y. G. C. A&A 707 A73 2026 et al.,
Gagné J., Faherty J. K., Schneider A. C., Meisner A. M., 2021, Astrophysics Source Code Library, record ascl:2106.007
Gaia Collaboration, 2020, VizieR Online Data Catalog: Gaia EDR3 (Gaia Collaboration, 2020), VizieR On-line Data Catalog: I/350
Gaia Collaboration, 2022, VizieR Online Data Catalog, p. I/355
Gaia Collaboration, 2023, A&A, 674, A1
Gan T. et al., 2023, AJ, 165, 17
Gan T., Theissen C. A., Wang S. X., Burgasser A. J., Mao S., 2025a, ApJS, 276, 47
Gan T. et al., 2025b, ApJ, 988, L78
Garcia L., Timmermans M., Pozuelos F. J., Ducrot E., Gillon M., Delrez L., Wells R. D., Jehin E., 2022, MNRAS, 509, 4817
Garcia L. J., Timmermans M., Pozuelos F. J., Ducrot E., Gillon M., Delrez L., Wells R. D., Jehin E., 2021, ASCLrecord ascl:2111.006
Ghachoui M. et al., 2024, A&A, 690, A263
Giacalone S. et al., 2021, AJ, 161, 24
Gillon M., Jehin E., Magain P., Chantry V., Hutsemékers D., Manfroid J., Queloz D., Udry S., 2011, EPJ Web of Conf., 11, 06002
Gizis J. E., 1997, AJ, 113, 806
Glusman R. I. AJ 2026 171 3 et al.,
Gravity Collaboration et al., 2019, A&A, 625, L10
Grether D., Lineweaver C. H., 2006, ApJ, 640, 1051
Grieves N. et al., 2017, MNRAS, 467, 4264
Guerrero N. M. et al., 2021, ApJS, 254, 39
Guillot T., Burrows A., Hubbard W. B., Lunine J. I., Saumon D., 1996, ApJ, 459, L35
Günther M. N., Daylan T., 2019, allesfitter: Flexible star and exoplanet inference from photometry and RV, preprint (ascl:1903.003)
Günther M. N., Daylan T., 2021, ApJS, 254, 13
Hamuy M., Walker A. R., Suntzeff N. B., Gigoux P., Heathcote S. R., Phillips M. M., 1992, PASP, 104, 533
Hamuy M., Suntzeff N. B., Heathcote S. R., Walker A. R., Gigoux P., Phillips M. M., 1994, PASP, 106, 566
Hartman J. D. et al., 2015, AJ, 149, 166
Hartman J. D. et al., 2023, AJ, 166, 163
Hartman J. D. et al., 2024, AJ, 168, 202
Hatzes A. P., 2019, The Doppler Method for the Detection of Exoplanets IOP Books Bristol978-0-7503-1687-3
Henry T. J., Jao W.-C., Subasavage J. P., Beaulieu T. D., Ianna P. A., Costa E., Méndez R. A., 2006, AJ, 132, 2360
Hippke M., Heller R., 2019, A&A, 623, A39
Hippke M., David T. J., Mulders G. D., Heller R., 2019, AJ, 158, 143
Hobson M. J. et al., 2023, ApJ, 946, L4
Hotnisky A. et al., 2025, AJ, 170, 1
Huang C., Wu Y., Triaud A. H. M. J., 2016, ApJ, 825, 98
Huang C. X. et al., 2020, Res. Notes Am. Astron. Soc., 4, 204
Husser T. O., Wende-von Berg S., Dreizler S., Homeier D., Reiners A., Barman T., Hauschildt P. H., 2013, A&A, 553, A6
Ida S., Lin D. N. C., 2004, ApJ, 604, 388
Ida S., Lin D. N. C., 2005, ApJ, 626, 1045
Iyer A. R., Line M. R., 2020, ApJ, 889, 78
Jackson B., Greenberg R., Barnes R., 2008, ApJ, 678, 1396
Janó Muñoz C. et al., 2025, MNRAS, 541, 630
Jehin E. et al., 2011, The Messenger, 145, 2
Jenkins J. M. et al., 2016, in Chiozzi G., Guzman J. C., eds, Proc. SPIE Conf. Ser. Vol. 9913, Software and Cyberinfrastructure for Astronomy IV. SPIE, Bellingham, p. 99133E
Jensen E., 2013, Astrophysics Source Code Library, record ascl:1306.007
Johnson J. A., Aller K. M., Howard A. W., Crepp J. R., 2010, PASP, 122, 905
Kagetani T. et al., 2023, PASJ, 75, 713
Kanodia S. et al., 2023, AJ, 165, 120
Kanodia S. et al., 2024, AJ, 167, 161
Kanodia S. et al., 2025, AJ, 170, 203
Kempton E. M. R. et al., 2018, PASP, 130, 114401
Kipping D. M., 2013, MNRAS, 435, 2152
Kunimoto M. et al., 2022, ApJS, 259, 33
Laughlin G., Bodenheimer P., Adams F. C., 2004, ApJ, 612, L73
Lépine S., Rich R. M., Shara M. M., 2003, AJ, 125, 1598
Li J., Tenenbaum P., Twicken J. D., Burke C. J., Jenkins J. M., Quintana E. V., Rowe J. F., Seader S. E., 2019, PASP, 131, 024506
Lightkurve Collaboration et al., 2018, Astrophysics Source Code Library, record ascl:1812.013
Lin D. N. C., Bodenheimer P., Richardson D. C., 1996, Nature, 380, 606
Lindegren L. et al., 2021, A&A, 649, A4
Lindgren S., Heiter U., 2017, A&A, 604, A97
Lissauer J. J., 1993, ARA&A, 31, 129
Liu B., Ji J., 2020, Res. Astron. Astrophys., 20, 164
Madhusudhan N., Bitsch B., Johansen A., Eriksson L., 2017, MNRAS, 469, 4102
Maldonado J. et al., 2023, A&A, 674, A132
Mann A. W., Brewer J. M., Gaidos E., Lépine S., Hilton E. J., 2013, AJ, 145, 52
Mann A. W., Feiden G. A., Gaidos E., Boyajian T., von Braun K., 2015, ApJ, 804, 64
Mann A. W. et al., 2019, ApJ, 871, 63
Marshall J. L. et al., 2008, in McLean I. S., Casali M. M., eds, Proc. SPIE Conf. Ser. Vol. 7014, Ground-based and Airborne Instrumentation for Astronomy II. SPIE, Bellingham, p. 701454
Mayor M., Queloz D., 1995, Nature, 378, 355
McCully C., Volgenau N. H., Harbeck D.-R., Lister T. A., Saunders E. S., Turner M. L., Siiverd R. J., Bowman M., 2018, in Proc. SPIE. p. 107070K, preprint (arXiv:1811.04163)
Mercer A., Stamatellos D., 2020, A&A, 633, A116
Miller J. S., Stone R. P. S., 1994, Technical Report 66, The Kast Double Spectrograph. University of California Lick Observatory Technical Reports
Miller N., Fortney J. J., 2011, ApJ, 736, L29
Minkowski R. L., Abell G. O., 1963, in Strand K. A., ed., Basic Astronomical Data: Stars and Stellar Systems. p. University of Chicago Press Chicago, IL 481
Mollière P. et al., 2022, ApJ, 934, 74
Morales J. C., Gallardo J., Ribas I., Jordi C., Baraffe I., Chabrier G., 2010, ApJ, 718, 502
Mordasini C., Alibert Y., Benz W., Naef D., 2008, in Fischer D., Rasio F. A., Thorsett S. E., Wolszczan A., eds, ASP Conf. Ser. Vol. 398, Extreme Solar Systems. Astron. Soc. Pac., San Francisco, p. 235
Mugrauer M., Rück J., Michel K.-U., 2023, Astron. Nachr., 344, e20230055
Murray C. A. et al., 2020, MNRAS, 495, 2446
Narita N. et al., 2019, J. Astron. Telesc. Instrum. Syst., 5, 015001
Öberg K. I., Murray-Clay R., Bergin E. A., 2011, ApJ, 743, L16
Oke J. B., 1990, AJ, 99, 1621
Parviainen H., Aigrain S., 2015, MNRAS, 453, 3821
Parviainen H. et al., 2019, A&A, 630, A89
Parviainen H. et al., 2021a, A&A, 645, A16
Parviainen H. et al., 2021b, A&A, 645, A16
Passegger V. M. et al., 2022, A&A, 658, A194

Paxton B. et al., 2015, ApJS, 220, 15
Pedersen P. P. et al., 2024, in Bryant J. J., Motohara K., Vernet J. R. D., eds, Proc. SPIE Conf. Ser. Vol. 13096, Ground-based and Airborne Instrumentation for Astronomy X. SPIE, Bellingham, p. 130963X
Pepe F. et al., 2021, A&A, 645, A96
Piso A.-M. A., Youdin A. N., Murray-Clay R. A., 2015, ApJ, 800, 82
Pollack J. B., Hubickyj O., Bodenheimer P., Lissauer J. J., Podolak M., Greenzweig Y., 1996, Icarus, 124, 62
Powell B. P. et al., 2022, Res. Notes Am. Astron. Soc., 6, 111
Prochaska J. X. et al., 2020a, pypeit/PypeIt: Release 1.0.0
Prochaska J. X., Hennawi J. F., Westfall K. B., Cooke R. J., Wang F., Hsyu T., Davies F. B., Farina E. P., 2020b, preprint (arXiv:2005.06505)
Prochaska J. X. et al., 2020c, J. Open Source Softw., 5, 2308
Rackham B. V., de Wit J., 2024, AJ, 168, 82
Rackham B. V., Apai D., Giampapa M. S., 2018, ApJ, 853, 122
Rackham B. V., Apai D., Giampapa M. S., 2019, AJ, 157, 96
Rackham B. V. et al., 2023, RAS Techniques and Instruments, 2, 148
Rafikov R. R., 2006, ApJ, 648, 666
Rasio F. A., Ford E. B., 1996, Science, 274, 954
Rayner J. T., Toomey D. W., Onaka P. M., Denault A. J., Stahlberger W. E., Vacca W. D., Cushing M. C., Wang S., 2003, PASP, 115, 362
Rayner J. T., Cushing M. C., Vacca W. D., 2009, ApJS, 185, 289
Reid I. N., Hawley S. L., Gizis J. E., 1995, AJ, 110, 1838
Reylé C., Jardine K., Fouqué P., Caballero J. A., Smart R. L., Sozzetti A., 2021, A&A, 650, A201
Ribas I. et al., 2023, A&A, 670, A139
Rice M. et al., 2022, AJ, 164, 104
Rojas-Ayala B., Covey K. R., Muirhead P. S., Lloyd J. P., 2012, ApJ, 748, 93
Sagynbayeva S., Farr W. M., Morris B. M., Luger R., 2025, ApJ, 990, 32
Sahlmann J. et al., 2011, A&A, 525, A95
Sanchis-Ojeda R., Winn J. N., Fabrycky D. C., 2013, Astron. Nachr., 334, 180
Schlafly E. F., Finkbeiner D. P., 2011, ApJ, 737, 103
Schlawin E. et al., 2014, in Ramsay S. K., McLean I. S., Takami H., eds, Proc. SPIE Conf. Ser. Vol. 9147, Ground-based and Airborne Instrumentation for Astronomy V. SPIE, Bellingham, p. 91472H
Schlegel D. J., Finkbeiner D. P., Davis M., 1998, ApJ, 500, 525
Schönrich R., Binney J., Dehnen W., 2010, MNRAS, 403, 1829
Sebastian D. et al., 2021, A&A, 645, A100
Sebastian D. et al., 2023, MNRAS, 519, 3546
Sebastian D. et al., 2024, MNRAS, 530, 2572
Sebastian D., Triaud A. H. M. J., Maxted P. F. L., Brogi M., 2025, Contributions of the Astronomical Observatory Skalnate Pleso, 55, 412
Sharma S. et al., 2018, MNRAS, 473, 2004
Skrutskie M. F. et al., 2006, AJ, 131, 1163
Smith J. C. et al., 2012, PASP, 124, 1000
Spada F., Demarque P., Kim Y. C., Sills A., 2013, ApJ, 776, 87
Speagle J. S., 2020, MNRAS, 493, 3132
Spitoni E., Silva Aguirre V., Matteucci F., Calura F., Grisoni V., 2019, A&A, 623, A60
Stassun K. G. et al., 2019, AJ, 158, 138
Stumpe M. C. et al., 2012, PASP, 124, 985
Stumpe M. C., Smith J. C., Catanzarite J. H., Van Cleve J. E., Jenkins J. M., Twicken J. D., Girouard F. R., 2014, PASP, 126, 100
Swayne M. I. et al., 2024, MNRAS, 528, 5703
Teske J. K., Thorngren D., Fortney J. J., Hinkel N., Brewer J. M., 2019, AJ, 158, 239
Thorngren D. P., Fortney J. J., Murray-Clay R. A., Lopez E. D., 2016, ApJ, 831, 64
Triaud A. H. M. J., 2018, in Deeg H. J., Belmonte J. A., eds, Handbook of Exoplanets. p. Springer International Publishing 2
Triaud A. H. M. J. et al., 2011, A&A, 531, A24
Triaud A. H. M. J. et al., 2013, A&A, 549, A18
Triaud A. H. M. J. et al., 2023, MNRAS, 525, L98
Turrini D. et al., 2021, ApJ, 909, 40
Twicken J. D. et al., 2018, PASP, 130, 064502
Valio A., Araújo A., 2022, ApJ, 940, 132
Walsh C., 2025, preprint (arXiv:2508.09587)
West A. A., Hawley S. L., Bochanski J. J., Covey K. R., Reid I. N., Dhital S., Hilton E. J., Masuda M., 2008, AJ, 135, 785
Wright J. T., Marcy G. W., Howard A. W., Johnson J. A., Morton T. D., Fischer D. A., 2012, ApJ, 753, 160
Zacharias N., Finch C. T., Girard T. M., Henden A., Bartlett J. L., Monet D. G., Zacharias M. I., 2013, AJ, 145, 44
Zanazzi J. J., Dewberry J., Chiang E., 2024, ApJ, 967, L29
Zechmeister M., Kürster M., 2009, A&A, 496, 577

APPENDIX A: TESS TARGET PIXEL FILES

In Fig. A1, we present a target pixel file for each of the stars in our sample where we used *TESS* photometry (TOI 5007, TOI 5292 A, and TOI-5916). Each has the SPOC pipeline aperture overplotted for reference.

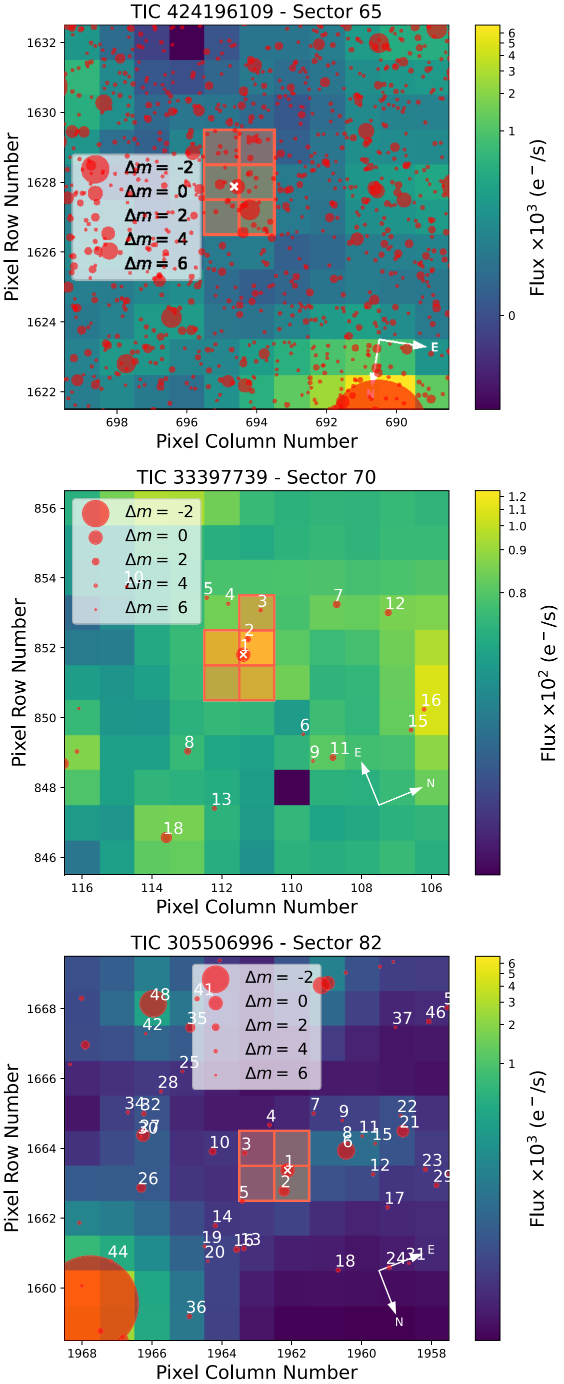

Figure A1. TESS target pixel files for TOI-5007 (left), TOI-5292 A (middle) and TOI-5916 (right). Red grids show default *TESS* apertures corresponding to the *TESS* photometry used in this work. For TOI-5292 A, only one sector's TPF is shown. Red circles depict other *Gaia* sources within the field, with sizes corresponded to their magnitude difference compared to the target star. For TOI-5007, we remove the labeling of these sources for visual clarity, as a result of the field being very crowded.

APPENDIX B: SUMMARY OF GROUND-BASED OBSERVATIONS

In Tables B1 and B2, we present a journal of our ground-based photometric observations collected for this work.

Table B1. Summary of ground-based follow-up observations obtained for TOI-3288 Ab, TOI-4666 b, and TOI-5007 b.

Observatory	Filter	Date	Coverage	Exposure (s)	FWHM (arcsec)	Aperture (arcsec)	Measurements
TOI-3288 Ab							
SSO/Callisto	*zYJ*	2022 Jun 30	Full	18	1.72	2.80	1290
SSO/Io	*Sloan-g′*	2022 Jul 10	Full	120	3.71	2.38	181
SSO/Europa	*Sloan-r′*	2022 Jul 20	Full	74	1.69	1.44	218
SSO/Callisto	*zYJ*	2022 Aug 05	Egress	44	1.84	4.00	339
SSO/Europa	*Sloan-g′*	2022 Aug 05	Egress	120	1.47	2.50	97
SSO/Io	$I+z$	2022 Aug 05	Egress	17	1.78	2.64	431
SSO/Io	$I+z$	2022 Aug 07	Secondary	17	1.47	2.23	1278
SSO/Callisto	*zYJ*	2022 Aug 12	Full	40	2.21	2.80	441
SSO/Europa	$I+z$	2022 Aug 12	Egress	17	1.28	2.16	961
SSO/Ganymede	*Sloan-r′*	2022 Aug 12	Full	74	2.47	3.33	212
SSO/Io	*Sloan-g′*	2022 Aug 12	Full	120	2.23	2.16	120
SSO/Callisto	*zYJ*	2022 Nov 12	Full	18	2.26	2.80	439
SSO/Io	*Sloan-g′*	2022 Nov 12	Full	112	2.15	0.61	68
SSO/Callisto	*Sloan-z′*	2023 Apr 07	Partial	27	2.08	2.66	368
SSO/Europa	*Sloan-r′*	2023 Apr 07	Partial	74	1.24	2.83	161
SSO/Ganymede	*Sloan-i′*	2023 Apr 07	Partial	37	1.36	3.45	290
SSO/Io	*Sloan-g′*	2023 Apr 07	Partial	120	1.84	2.13	104
TRAPPIST-South	$I+z$	2023 Sep 12	Full	60	2.87	4.14	200
SSO/Callisto	*zYJ*	2025 Sep 15	Full	18	1.56	2.80	931
TOI-4666 b							
SSO/Europa	$I+z$	2022 Oct 10	Full	16	1.45	2.32	822
SSO/Callisto	*zYJ*	2022 Dec 16	Full	16	2.38	2.80	1412
SSO/Europa	*Sloan-r′*	2022 Dec 16	Egress	70	1.53	2.83	217
SSO/Ganymede	*Sloan-z′*	2022 Dec 16	Egress	25	1.35	3.17	488
SSO/Io	*Sloan-g′*	2022 Dec 16	Egress	160	1.87	2.05	115
SSO/Callisto	*zYJ*	2023 Jan 17	Full	16	2.31	2.80	1212
SSO/Europa	*Sloan-g′*	2023 Jan 17	Full	160	1.36	2.52	111
SSO/Ganymede	*Sloan-r′*	2023 Jan 17	Full	70	1.44	1.94	246
TRAPPIST-South	*Sloan-z′*	2023 Jan 17	Full	130	2.52	3.40	118
SSO/Callisto	$I+z$	2023 Sep 08	Secondary	16	2.55	4.71	822
SSO/Europa	*Sloan-i′*	2023 Sep 08	Secondary	35	1.73	3.21	476
SSO/Europa	*Sloan-i′*	2023 Sep 24	Full	35	1.27	2.04	493
SSO/Io	$I+z$	2023 Sep 24	Full	16	1.93	3.09	927
SSO/Europa	$I+z$	2023 Oct 13	Secondary	16	1.26	2.33	521
TRAPPIST-South	*Sloan-z′*	2024 Dec 18	Full	120	2.32	6.03	144
TOI-5007 b							
TRAPPIST-South	$I+z$	2022 May 02	Full	60	1.93	3.52	209
TRAPPIST-South	$I+z$	2022 Jul 02	Full	110	2.58	3.26	140
SSO/Io	*Sloan-g′*	2022 Aug 27	Full	120	1.79	1.94	114
TRAPPIST-South	*Sloan-z′*	2023 Feb 03	Full	110	2.61	3.3	89
SSO/Europa	*Sloan-i′*	2023 May 26	Full	44	1.18	1.27	317
SSO/Europa	*Sloan-r′*	2025 Mar 12	Ingress	88	1.01	1.27	78
SSO/Ganymede	*Sloan-z′*	2025 Mar 12	Full	32	2.15	2.61	263
SSO/Callisto	*zYJ*	2025 Sep 14	Full	40	2.25	2.80	176
LCO-SSO−0m4	*Sloan-r′*	2023 Apr 21	Ingress	600	5.19	3.40	12
ExTrA/T3	$1.41\ \mu m$	2022 May 22	Full	60	1.38	8.00	163
ExTrA/T2	$1.41\ \mu m$	2022 July 02	Full	60	1.48	8.00	330
ExTrA/T2	$1.41\ \mu m$	2022 Aug 27	Full	60	1.23	8.00	218
ExTrA/T1+T2 + T3	$1.41\ \mu m$	2023 Apr 28	Full	60	1.40	8.00	218
ExTrA/T1+T2 + T3	$1.41\ \mu m$	2023 May 03	Full	60	1.69	8.00	143
ExTrA/T1+T2 + T3	$1.41\ \mu m$	2023 May 21	Partial	60	1.51	8.00	119
ExTrA/T1+T2 + T3	$1.41\ \mu m$	2023 May 26	Full	60	1.33	8.00	207
ExTrA/T1+T2 + T3	$1.41\ \mu m$	2023 May 31	Full	60	1.41	8.00	218
ExTrA/T1+T2 + T3	$1.41\ \mu m$	2023 Jul 16	Full	60	1.67	8.00	237
ExTrA/T1+T2 + T3	$1.41\ \mu m$	2023 Aug 13	Full	60	1.22	8.00	191
ExTrA/T1 + T2	$1.41\ \mu m$	2023 Aug 26	Full	60	1.46	8.00	257

Table B2. Summary of ground-based follow-up observations obtained for TOI-5292 Ab and TOI-5916 b.

Observatory	Filter	Date	Coverage	Exposure (s)	FWHM (arcsec)	Aperture (arcsec)	Measurements
			TOI-5292 Ab				
TRAPPIST-North	$I+z$	2023 Dec 09	Egress	120	2.13	2.77	93
TRAPPIST-North	*Sloan*-z'	2023 Dec 11	Full	150	2.43	2.63	69
SNO/Artemis	*Sloan*-g'	2024 Sep 27	Full	160	1.37	1.94	87
SNO/Artemis	*Sloan*-z'	2024 Oct 03	Full	60	1.54	1.83	193
SNO/Artemis	*Sloan*-z'	2024 Dec 18	Full secondary	60	2.26	1.39	75
SNO/Artemis	*Sloan*-i'	2024 Dec 19	Full	120	1.51	2.33	77
			TOI-5916 b				
SNO/Artemis	*Sloan*-g'	2022 Nov 28	Full	140	1.21	1.12	85
TRAPPIST-North	$I+z$	2022 Nov 28	Full	120	2.27	3.58	114
TCS-MuSCAT2	g'	2024 Aug 16	Full	50	–	6.96	227
TCS-MuSCAT2	r'	2024 Aug 16	Full	50	–	6.96	231
TCS-MuSCAT2	i'	2024 Aug 16	Full	15	–	6.96	732
TCS-MuSCAT2	zs'	2024 Aug 16	Full	50	–	6.96	231

APPENDIX C: ARCHIVAL IMAGING

In Fig. C1, we present the archival images described in Section 4.1.

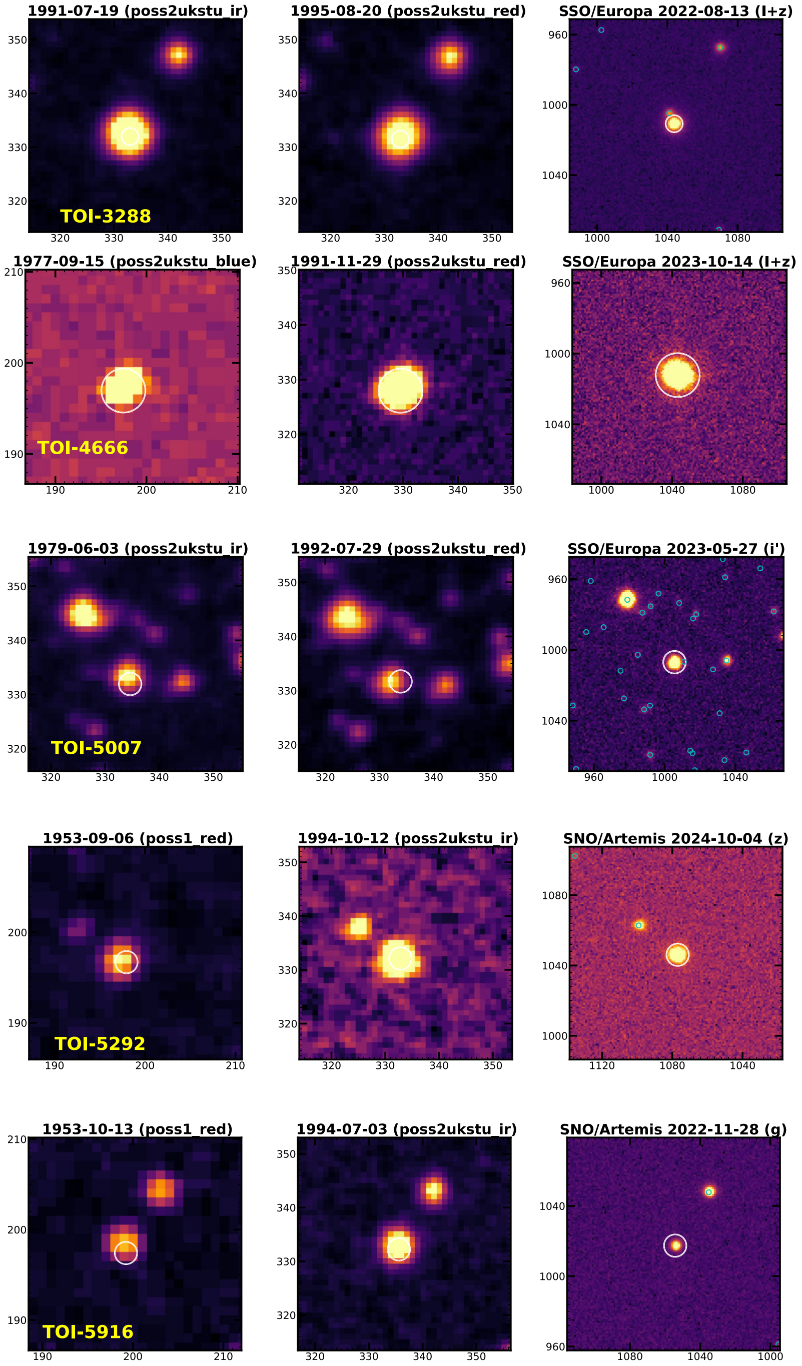

Figure C1. Archival images for the systems discussed in the paper. From top to bottom, the row of three images show: TOI-3288 A, TOI-4666, TOI-5007, TOI-5292 A, and TOI-5916. Each plot is titled with the date and instrument used to take the image. White circles show the position of each respective star at its most recent image position (i.e. in the SPECULOOS images), thus showing how its position has evolved.

APPENDIX D: SED FITS

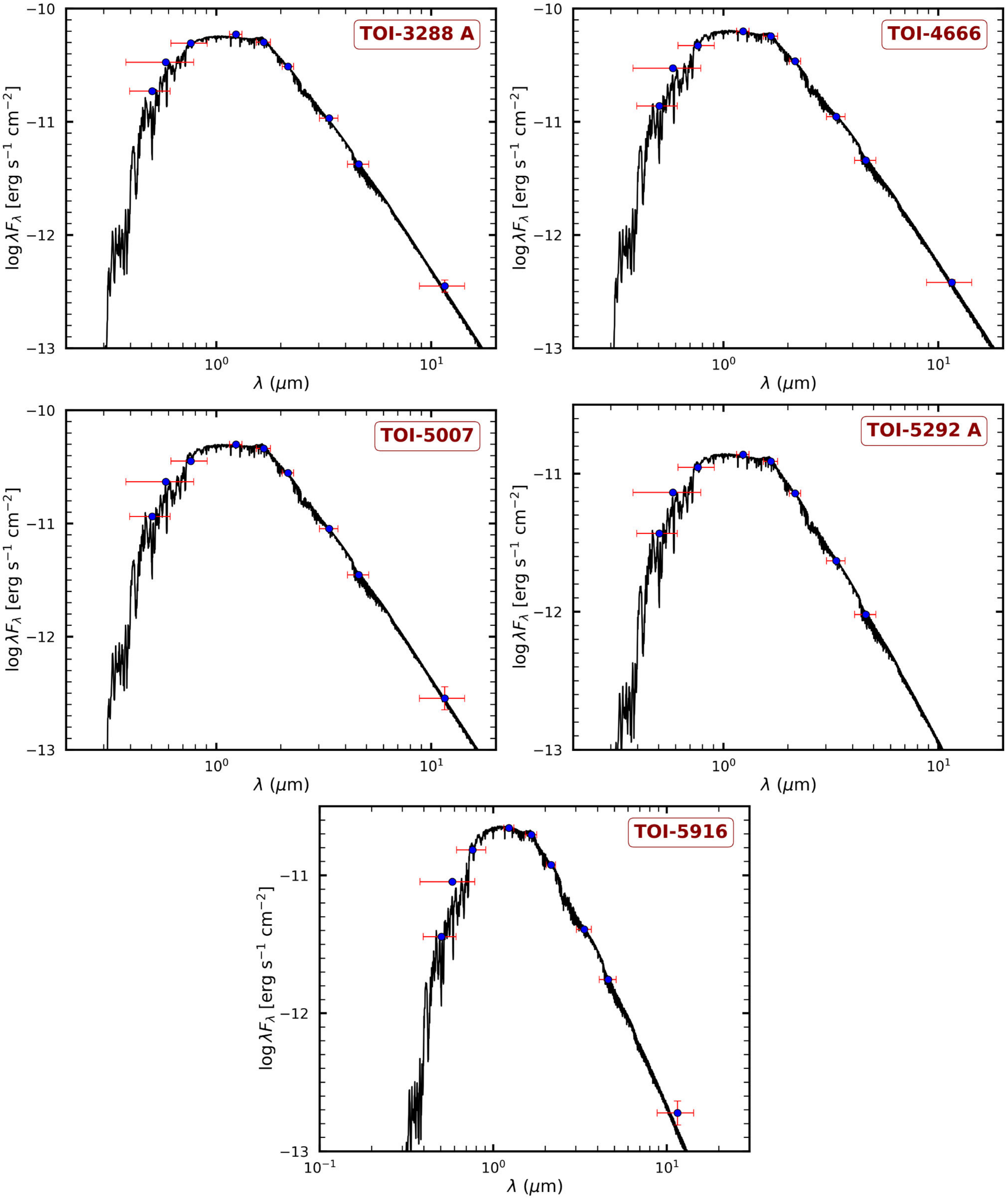

Figure D1. SED for TOI-3288 A, TOI-4666, TOI-5007, TOI-5292 A, and TOI-5916. The red symbols represent the observed photometric measurements, and the horizontal bars represent the effective width of the passband.

APPENDIX E: RV DATASETS

We present the RV points collected with ESPRESSO and PFS for the confirmation of the planets in this work. Points for TOI-3288 A are provided in Table E1, TOI-4666 in Table E2, TOI-5292 A in Table E3, TOI-5916 in Table E4, and TOI-5007 in Table E5.

Table E1. RV measurements obtained with ESPRESSO for TOI-3288 A.

Time (BJD)	RV (km.s^{-1})	Error (km.s^{-1})
2460588.59382091	29.642753	0.028918
2460589.58301817	28.930989	0.020481
2460591.53703018	29.710953	0.049006
2460596.55754534	28.877204	0.020749
2460764.88300042	29.537801	0.021033
2460927.5789118	29.1194043	0.022688

Table E2. RV measurements obtained with ESPRESSO for TOI-4666.

Time (BJD)	RV (km.s^{-1})	Error (km.s^{-1})
2460296.54909425	7.873443	0.018208
2460611.60882457	7.715562	0.016224
2460612.75344893	7.801105	0.013576
2460613.62217581	7.895610	0.028190
2460614.60423935	7.705984	0.037956

Table E3. RV measurements obtained with ESPRESSO for TOI-5292 A.

Time (BJD)	RV (km.s^{-1})	Error (km.s^{-1})
2460819.88751442	−8.543389	0.016603
2460837.82802106	−8.389539	0.017020
2460850.7915149	−8.9525730	0.025503
2460867.8634546	−8.4141739	0.013828
2460880.89505529	−8.853235	0.014809
2460895.72150212	−8.821266	0.019857

Table E4. RV measurements obtained with ESPRESSO for TOI-5916.

Time (BJD)	RV (km.s^{-1})	Error (km.s^{-1})
2460587.64343877	−2.227842	0.022585
2460588.5093216	−1.919660	0.024024
2460589.57345587	−2.145545	0.020670
2460594.60454244	−2.169590	0.038107
2460595.52760945	−1.939142	0.017934

Table E5. RV measurements obtained with ESPRESSO (top) and PFS (bottom) for TOI-5007.

Time (BJD)	RV (km.s^{-1})	Error (km.s^{-1})
2460728.82822461	4.506280	0.017591
2460731.84552939	4.617750	0.025800
2460735.79607892	4.365100	0.016645
2460736.85480744	4.604084	0.033525
2460042.84358	0.15931	0.01152
2460042.85728	0.16258	0.01183
2460042.87098	0.15394	0.01051
2460043.82899	−0.13012	0.01167
2460043.84350	−0.13319	0.01128
2460043.85775	−0.08936	0.01199
2460044.82447	0.06492	0.01176
2460044.83907	0.05545	0.01314
2460044.85367	0.03082	0.01207
2460063.75571	−0.01956	0.01572
2460063.77096	−0.01524	0.01331
2460063.78556	−0.0178	0.01180
2460067.76870	0.06425	0.01436
2460067.78289	0.06838	0.01499
2460067.79737	0.10587	0.01439
2460509.52196	−0.08646	0.01189
2460509.53575	−0.09951	0.01101
2460509.55012	−0.11911	0.01171
2460517.50560	0.00900	0.0174
2460517.52053	−0.04869	0.0181
2460517.53594	0.0000	0.01712

APPENDIX F: ADDITIONAL FITTED PARAMETERS

In these Tables we present additional fitted and derived parameters (dilutions, RV jitter, and quadratic limb darkening coefficients) for the planets in our sample. Parameters for TOI-3288 Ab can be found in Table F1, TOI-4666 b in Table F2, TOI-5007 b in Table F3, TOI-5292 Ab in Table F4, and TOI-5916 b in Table F5.

Table F1. Fitted dilution coefficients for the contamination of TOI-3288 A by its bound companion TOI-3288 B, as well as RV jitter and derived quadratic limb darkening coefficients for TOI-3288 Ab.

Parameter	Value
Dilution TS $I+z$	$0.006^{+0.005}_{-0.008}$
Dilution SSO/Europa $I+z$	$0.013^{+0.009}_{-0.013}$
Dilution SSO/Io $I+z$	$0.079^{+0.020}_{-0.014}$
Dilution SSO/Callisto *Sloan-z'*	$0.044^{+0.025}_{-0.027}$
Dilution SSO/Europa *Sloan-r'*	$0.004^{+0.003}_{-0.005}$
Dilution SSO/Ganymede *Sloan-r'*	$0.007^{+0.005}_{-0.008}$
Dilution SSO/Ganymede *Sloan-i'*	$0.065^{+0.022}_{-0.019}$
Dilution SSO/Callisto/SPIRIT1 zYJ	$0.088^{+0.011}_{-0.008}$
Dilution SSO/Callisto/SPIRIT2 zYJ	$0.097^{+0.004}_{-0.002}$
Quadratic limb-darkening coefficient $u_{1,i'}$	$0.3863\ ^{0.0433}_{-0.0477}$
Quadratic limb-darkening coefficient $u_{2,i'}$	$0.1715\ ^{0.0552}_{-0.0474}$
Quadratic limb-darkening coefficient $u_{1,z'}$	$0.2589\ ^{0.0421}_{-0.0411}$
Quadratic limb-darkening coefficient $u_{2,z'}$	$0.1990\ ^{+0.0499}_{-0.0457}$
Quadratic limb-darkening coefficient $u_{1,r'}$	$0.6896\ ^{+0.0417}_{-0.0390}$
Quadratic limb-darkening coefficient $u_{2,r'}$	$0.0094\ ^{+0.0492}_{-0.0491}$
Quadratic limb-darkening coefficient $u_{1,I+z}$	$0.3824\ ^{+0.0419}_{-0.0388}$
Quadratic limb-darkening coefficient $u_{2,I+z}$	$0.1671\ ^{+0.0498}_{-0.0491}$
Quadratic limb-darkening coefficient $u_{1,g'}$	$0.6725\ ^{+0.0566}_{-0.0513}$
Quadratic limb-darkening coefficient $u_{2,g'}$	$0.0790\ ^{+0.0545}_{-0.0547}$
Quadratic limb-darkening coefficient $u_{1,zYJ}$	$0.2623\ ^{0.0362}_{-0.0355}$
Quadratic limb-darkening coefficient $u_{2,zYJ}$	$0.1523\ ^{0.0400}_{-0.0403}$
$\ln \sigma_{\mathrm{jitter;ESPRESSO}}$ (km s^{-1})	$-9.0^{+3.2}_{-3.5}$

Table F2. Fitted limb darkening coefficients and RV jitter for TOI-4666 b.

Parameter	Value
Quadratic limb-darkening coefficient $u_{1,i'}$	$0.4212\,^{0.0390}_{-0.0367}$
Quadratic limb-darkening coefficient $u_{2,i'}$	$0.1744\,^{0.0498}_{0.0501}$
Quadratic limb-darkening coefficient $u_{1,z'}$	$0.3333\,^{0.0365}_{0.0351}$
Quadratic limb-darkening coefficient $u_{2,z'}$	$0.1602\,^{+0.0442}_{-0.0445}$
Quadratic limb-darkening coefficient $u_{1,r'}$	$0.5882\,^{+0.0432}_{-0.0420}$
Quadratic limb-darkening coefficient $u_{2,r'}$	$0.1268\,^{+0.0564}_{-0.0568}$
Quadratic limb-darkening coefficient $u_{1,I+z}$	$0.3930\,^{+0.0300}_{-0.0284}$
Quadratic limb-darkening coefficient $u_{2,I+z}$	$0.1323\,^{+0.0441}_{-0.0423}$
Quadratic limb-darkening coefficient $u_{1,g'}$	$0.5857\,^{+0.0493}_{-0.0494}$
Quadratic limb-darkening coefficient $u_{2,g'}$	$0.1690\,^{+0.0582}_{-0.0577}$
Quadratic limb-darkening coefficient $u_{1,zYJ}$	$0.2290\,^{+0.0280}_{-0.0287}$
Quadratic limb-darkening coefficient $u_{2,zYJ}$	$0.1959\,^{+0.0451}_{-0.0427}$
$\ln \sigma_{\rm jitter;ESPRESSO}$ (km s^{-1})	-9.5 ± 3.6

Table F3. Fitted limb darkening coefficients and RV jitter for TOI-5007 b.

Parameter	Value
Dilution TESS	$0.724 \pm +0.015$
Quadratic limb-darkening coefficient $u_{1,TESS}$	$0.3421^{0.0544}_{-0.0519}$
Quadratic limb-darkening coefficient $u_{2,TESS}$	$0.2003^{0.0477}_{-0.0496}$
Quadratic limb-darkening coefficient $u_{1,i'}$	$0.3966^{0.0607}_{-0.0541}$
Quadratic limb-darkening coefficient $u_{2,i'}$	$0.1990^{0.0545}_{-0.0564}$
Quadratic limb-darkening coefficient $u_{1,z'}$	$0.2498^{0.0566}_{0.0511}$
Quadratic limb-darkening coefficient $u_{2,z'}$	$0.1595^{0.0480}_{0.0434}$
Quadratic limb-darkening coefficient $u_{1,r'}$	$0.5239^{0.0688}_{0.0663}$
Quadratic limb-darkening coefficient $u_{2,r'}$	$0.1771^{0.0658}_{0.0666}$
Quadratic limb-darkening coefficient $u_{1,g'}$	$0.6271^{0.0836}_{0.0760}$
Quadratic limb-darkening coefficient $u_{2,g'}$	$0.1434^{0.0700}_{0.0810}$
Quadratic limb-darkening coefficient $u_{1,ExTrA}$	$0.1767^{0.0495}_{0.0525}$
Quadratic limb-darkening coefficient $u_{2,ExTrA}$	$0.1214^{0.04617}_{0.0431}$
Quadratic limb-darkening coefficient $u_{1,zYJ}$	$0.2678^{0.1023}_{0.0931}$
Quadratic limb-darkening coefficient $u_{2,zYJ}$	$0.1470^{0.1019}_{0.0817}$
$\ln \sigma_{\rm jitter;ESPRESSO}$ (km s^{-1})	$-10.1^{3.7}_{3.2}$
$\ln \sigma_{\rm jitter;PFS}$ (km s^{-1})	$-4.1^{0.2}_{0.3}$

Table F4. Fitted limb darkening coefficients and RV jitter for TOI-5292 Ab.

Parameter	Value
Quadratic limb-darkening coefficient $u_{1,TESS}$	$0.3639\,^{0.0620}_{-0.0563}$
Quadratic limb-darkening coefficient $u_{2,TESS}$	$0.1801\,^{0.0566}_{0.0546}$
Quadratic limb-darkening coefficient $u_{1,I+z}$	$0.2871\,^{0.0552}_{-0.0514}$
Quadratic limb-darkening coefficient $u_{2,I+z}$	$0.1726\,^{0.0522}_{0.0488}$
Quadratic limb-darkening coefficient $u_{1,z'}$	$0.2911\,^{0.0511}_{0.0485}$
Quadratic limb-darkening coefficient $u_{2,z'}$	$0.1738\,^{+0.0505}_{-0.0477}$
Quadratic limb-darkening coefficient $u_{1,g'}$	$0.5610\,^{+0.0708}_{-0.0707}$
Quadratic limb-darkening coefficient $u_{2,g'}$	$0.1771\,^{+0.0692}_{-0.0672}$
Quadratic limb-darkening coefficient $u_{1,i'}$	$0.3762\,^{+0.0579}_{-0.0567}$
Quadratic limb-darkening coefficient $u_{2,i'}$	$0.1816\,^{+0.0569}_{-0.0546}$
$\ln \sigma_{\rm jitter;ESPRESSO}$ (km s^{-1})	$-9.2^{+3.5}_{-3.8}$

Table F5. Fitted limb darkening coefficients and RV jitter for TOI-5916 b.

Parameter	Value
Quadratic limb-darkening coefficient $u_{1,TESS}$	$0.2804\,^{0.0494}_{-0.0469}$
Quadratic limb-darkening coefficient $u_{2,TESS}$	$0.2062\,^{0.0490}_{0.0440}$
Quadratic limb-darkening coefficient $u_{1,g'}$	$0.5287\,^{0.0597}_{-0.0610}$
Quadratic limb-darkening coefficient $u_{2,g'}$	$0.2304\,^{0.0617}_{0.0586}$
Quadratic limb-darkening coefficient $u_{1,I+z}$	$0.2657\,^{0.0463}_{0.0444}$
Quadratic limb-darkening coefficient $u_{2,I+z}$	$0.1904\,^{+0.0432}_{-0.0420}$
Quadratic limb-darkening coefficient $u_{1,r'}$	$0.5381\,^{+0.0663}_{-0.0614}$
Quadratic limb-darkening coefficient $u_{2,r'}$	$0.1824\,^{+0.0651}_{-0.0634}$
Quadratic limb-darkening coefficient $u_{1,z'}$	$0.2514\,^{+0.0471}_{-0.0466}$
Quadratic limb-darkening coefficient $u_{2,z'}$	$0.1651\,^{+0.0421}_{-0.0395}$
Quadratic limb-darkening coefficient $u_{1,zs}$	$0.2625\,^{+0.0507}_{-0.0461}$
Quadratic limb-darkening coefficient $u_{2,zs}$	$0.2037\,^{+0.0466}_{-0.0457}$
Quadratic limb-darkening coefficient $u_{1,i'}$	$0.3384\,^{+0.0501}_{-0.0525}$
Quadratic limb-darkening coefficient $u_{2,i'}$	$0.1977\,^{+0.0505}_{-0.0470}$
$\ln \sigma_{\rm jitter;ESPRESSO}$ (km s^{-1})	$-6.6^{+2.3}_{-3.1}$

[1] *Department of Astrophysics, University of Oxford, Denys Wilkinson Building, Keble Road, Oxford OX1 3RH, UK*
[2] *Magdalen College, University of Oxford, Oxford OX1 4AU, UK*
[3] *School of Physics & Astronomy, University of Birmingham, Edgbaston, Birmingham B15 2TT, UK*
[4] *Astrobiology Research Unit, Université de Liège, 19C Allée du 6 Août, B-4000 Liège, Belgium*
[5] *Thüringer Landessternwarte Tautenburg, Sternwarte 5, D-07778, Tautenburg, Germany*
[6] *Department of Earth, Atmospheric and Planetary Sciences, Massachusetts Institute of Technology, 77 Massachusetts Avenue, Cambridge, MA 02139, USA*
[7] *Kavli Institute for Astrophysics and Space Research, Massachusetts Institute of Technology, Cambridge, MA 02139, USA*
[8] *Department of Astronomy & Astrophysics, UC San Diego, 9500 Gilman Drive, La Jolla, CA 92093, USA*
[9] *Instituto de Astrofísica de Canarias (IAC), Calle Vía Láctea s/n, E-38200, La Laguna, Tenerife, Spain*
[10] *Univ. Grenoble Alpes, CNRS, IPAG, F-38000 Grenoble, France*
[11] *Observatoire de Genève, Département d'Astronomie, Université de Genève, Chemin Pegasi 51b, CH-1290 Versoix, Switzerland*
[12] *School of Physics and Astronomy, University of Leicester, University Road, Leicester LE1 7RH, UK*
[13] *Center for Astrophysics |Harvard & Smithsonian, 60 Garden Street, Cambridge, MA 02138, USA*
[14] *Komaba Institute for Science, The University of Tokyo, 3-8-1 Komaba, Meguro, Tokyo 153-8902, Japan*
[15] *Astrobiology Center, 2-21-1 Osawa, Mitaka, Tokyo 181-8588, Japan*
[16] *Cavendish Laboratory, JJ Thomson Avenue, Cambridge CB3 0HE, UK*
[17] *Carnegie Science Earth and Planets Laboratory, 5241 Broad Branch Road, NW, Washington, DC 20015, USA*
[18] *Deptartamento de Astrofísica, Universidad de La Laguna (ULL), E-38206 La Laguna, Tenerife, Spain*
[19] *Department of Astrophysical Sciences, Princeton University, 4 Ivy Lane, Princeton, NJ 08544, USA*
[20] *NSF Graduate Research Fellow, MIT Presidential Fellow, MIT CollamoreRogers Fellow, MIT Teaching Development Fellow*
[21] *Department of Applied Physics and Astronomy, and Sharjah Academy for Astronomy, Space Sciences and Technology, University of Sharjah, Sharjah, United Arab Emirates*
[22] *Cadi Ayyad University, Oukaimeden Observatory, High Energy Physics, Astrophysics and Geoscience Laboratory, FSSM, Marrakesh, Morocco*
[23] *SETI Institute, Mountain View, CA 94043,USA*

[24] *The Observatories of the Carnegie Institution for Science, 813 Santa Barbara Street, Pasadena, CA 91101,USA*
[25] *Center for Space and Habitability, University of Bern, Gesellschaftsstrasse 6, CH-3012 Bern, Switzerland*
[26] *Paris Region Fellow, Marie Sklodowska-Curie Action*
[27] *AIM, CEA, CNRS, Université Paris-Saclay, Université de Paris, F-91191 Gif-sur-Yvette, France*
[28] *Instituto de Astronomía, Universidad Nacional Autónoma de México, AP 70-264, Ciudad de México, 04510, México*
[29] *Space Sciences, Technologies and Astrophysics Research (STAR) Institute, Université de Liége, Allée du 6 Août 19C, B-4000 Liége, Belgium*
[30] *Department of Astrophysical and Planetary Sciences, University of Colorado Boulder, Boulder, CO 80309, USA*
[31] *Institute for Particle Physics and Astrophysics, ETH Zürich, Wolfgang-Pauli-Strasse 2, CH-8093 Zürich, Switzerland*
[32] *Instituto de Astrofísica de Andalucía (IAA-CSIC), Glorieta de la Astronomía s/n, E-18008 Granada, Spain*
[33] *Department of Astronomy, Yale University, 219 Prospect Street, New Haven, CT 06511, USA*
[34] *Department of Astronomy, McPherson Laboratory, The Ohio State University, 140 W 18th Avenue, Columbus, Ohio 43210, USA*

This paper has been typeset from a TEX/LATEX file prepared by the author.